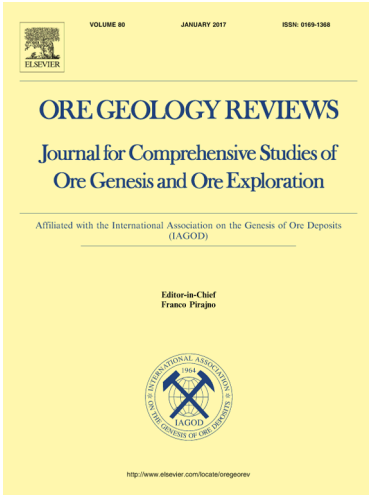

Intermediate sulfidation type base metal mineralization at Aliabad-Khanchy, Tarom-Hashtjin metallogenic belt, NW Iran

Hossein Kouhestani, Mir Ali Asghar Mokhtari, Zhaoshan Chang, Craig A. Johnson

PII: S0169-1368(17)30660-1
DOI: https://doi.org/10.1016/j.oregeorev.2017.12.012
Reference: OREGEO 2432

To appear in: *Ore Geology Reviews*

Received Date: 27 August 2017
Revised Date: 7 December 2017
Accepted Date: 11 December 2017

Please cite this article as: H. Kouhestani, M.A.A. Mokhtari, Z. Chang, C.A. Johnson, Intermediate sulfidation type base metal mineralization at Aliabad-Khanchy, Tarom-Hashtjin metallogenic belt, NW Iran, *Ore Geology Reviews* (2017), doi: https://doi.org/10.1016/j.oregeorev.2017.12.012

Intermediate sulfidation type base metal mineralization at Aliabad-Khanchy, Tarom-Hashtjin metallogenic belt, NW Iran

Hossein Kouhestani [a,*], Mir Ali Asghar Mokhtari [a], Zhaoshan Chang [b], Craig A. Johnson [c]

[a] *Department of Geology, Faculty of Sciences, University of Zanjan, Zanjan 45195–313, Iran*

[b] *EGRU (Economic Geology Research Centre) and Academic Group of Geosciences, College of Science and Engineering, James Cook University, Townsville, Queensland 4811, Australia*

[c] *U.S. Geological Survey, Denver Federal Center, Denver, CO 80225, USA*

*Corresponding author at: Department of Geology, Faculty of Sciences, University of Zanjan, Zanjan 45195–313, Iran. Tel: +98 24 33054039.

E-mail address: kouhestani@znu.ac.ir (H. Kouhestani)

ABSTRACT

The Aliabad-Khanchy epithermal base metal deposit is located in the Tarom-Hashtjin metallogenic belt (THMB) of northwest Iran. The mineralization occurs as Cu-bearing brecciated quartz veins hosted by Eocene volcanic and volcaniclastic rocks of the Karaj Formation. Ore formation can be divided into five stages, with most ore minerals, such as pyrite and chalcopyrite being formed in the early stages. The main wall-rock alteration is silicification, and chlorite, argillic and propylitic alteration. Microthermometric measurements of fluid inclusion assemblages show that the ore-forming fluids have eutectic temperatures between −30° and −52°C, trapping temperatures of 150° to 290°C, and salinities of 6.6 to 12.4 wt.% NaCl equiv. These data demonstrate that the ore-forming fluids were medium- to high-temperature, medium- to low-salinity, and low-density H_2O–NaCl–$CaCl_2$ fluids. Calculated $\delta^{18}O$ values indicate that ore-forming hydrothermal fluids had $\delta^{18}O_{water}$ ranging from +3.6 to +0.8‰, confirming that the ore–fluid system evolved from dominantly magmatic to dominantly meteoric. The calculated $^{34}S_{H2S}$ values range from –8.1 to –5.0‰, consistent with derivation of the sulfur from either magma or possibly from local volcanic wall-rock. Combined, the fluid inclusion and stable isotope data indicate that the Aliabad-Khanchy deposit formed from magmatic-hydrothermal fluids. After rising to a depth of between 790 and 500 m, the fluid boiled and subsequent hydraulic fracturing may have led to inflow and/or mixing of early magmatic fluids with circulating groundwater causing deposition of base metals due to dilution and/or cooling. The Aliabad-Khanchy deposit is interpreted as an intermediate-sulfidation style of epithermal mineralization.

Our data suggest that the mineralization at Aliabad-Khanchy and other epithermal deposits of the THMB formed by hydrothermal activity related to shallow late Eocene magmatism. The altered Eocene volcanic and volcaniclastic rocks, especially at the intersection of subvolcanic stocks with faults were the most favorable sites for epithermal ore bodies in the THMB.

Keywords: Intermediate-sulfidation; fluid inclusions; stable isotopes; Aliabad-Khanchy; Tarom-Hashtjin metallogenic belt; Iran

1. Introduction

The Aliabad-Khanchy epithermal base metal deposit, a small-sized (0.2 Mt averaging 1.3% Cu) deposit, is located in the Tarom-Hashtjin metallogenic belt (THMB) approximately 30 km east of the city of Zanjan, northwestern Iran (Fig. 1). The THMB, which is 50–150-km-wide and 300-km-long, is a part of the Alborz magmatic arc (Alavi, 1991) and appears to be related to a waning phase of the Eocene to late Eocene magmatism. The magmatic rocks are high-K calc-alkaline to alkaline (Moayyed, 2001; Aghazadeh et al., 2011; Asiabanha and Foden, 2012; Castro et al., 2013; Nabatian et al., 2014a, 2016), and are tectonically linked to subduction of Khoy-Zanjan oceanic crust beneath the Alborz-Azarbaijan plate (Azizi and Jahangiri, 2008).

Besides the Aliabad-Khanchy deposit, several other epithermal deposits of precious and base metal are found in the THMB (Fig. 1B) including Chodarchay (0.5 Mt averaging 0.9% Cu and 2 g/t Au; Yasami et al., 2017); Gulojeh (2.3 Mt averaging 3% Pb, 2.2% Zn, 1.5% Cu, 2.9 g/t Au, and 350 g/t Ag; Mehrabi et al., 2010, 2016; Ghasemi Siani et al., 2015); Khalyfehlou (60,000 tonnes averaging 8% Cu, 6 g/t Au, and 7 g/t Ag; Esmaeli et al., 2015; Hosseinzadeh et al., 2016), Lohneh (Rahmani, 2010; Zamanian et al., 2016), Rashtabad, Jalilabad and Aqkand (Feizi et al., 2016; Kouhestani et al., 2017), and the iron oxide-apatite deposits at Sorkhe-Dizaj, Aliabad, Morvarid and Zaker (Nabatian and Ghaderi, 2013; Nabatian et al., 2013, 2014b). These deposits are controlled by normal faults and temporally and spatially associated with late Eocene magmatism. $^{40}Ar/^{39}Ar$ ages presented by Ghasemi Siani et al. (2015) and Mehrabi et al. (2016) indicated that Gulojeh deposit is formed at 42.20 ± 0.34 Ma which is temporally coincident with that of granodiorite stocks emplacement at 41.87 ± 1.58 Ma.

Except for small-scale geological maps of the area, i.e., 1:250,000 geological map of Zanjan (Stöcklin and Eftekheārnezhād, 1969) and 1:100,000 geological map of Tarom (Amini et al., 2001) and a number of unpublished company exploration reports (Kan Iran Exploration Co., 1999; Kouhestani and Mokhtari, 2013a), studies of the Aliabad-Khanchy mineralization have been limited and include publications by

Kouhestani and Mokhtari (2013b), Mokhtari et al. (2016) and Saeedi et al. (2017). However, these studies provide little insight into the origin of the deposit. In this paper, we describe the geological setting and geochemical characteristics of the Aliabad-Khanchy deposit, including fluid inclusions and stable isotopic characteristics, propose a genetic model for the deposit and guidelines for future exploration in the THMB. Our results extend knowledge of the epithermal mineralization processes at the THMB, and provide exploration criteria for similar epithermal ores in this area and other parts of the Alborz magmatic arc in northwestern Iran.

2. Geological setting

Magmatism in the THMB began during the Eocene and continued through the late Eocene (Amini et al., 2001; Nabatian and Ghaderi, 2013; Nabatian et al., 2014a, 2016). This belt comprises mostly Eocene volcanic and sedimentary rocks intruded by late Eocene plutonic rocks (Fig. 1B). The Eocene submarine volcanism consists of pyroclastic rocks with interbedded limestone and sandstone towards the base, and lava flows of trachyte, trachyandesite, andesite, basaltic andesite, olivine basalt, and porphyritic and non-porphyritic rhyodacite towards the top. Hirayama et al. (1966) grouped all the Eocene volcanic and sedimentary rocks in the THMB as "Karaj Formation", and Verdel et al. (2011) dated the rocks at 49.3±2.9 Ma to 41.1±1.6 Ma based on zircon U–Pb dating of tuff units. The plutonic rocks vary in composition from microdiorite, quartz-monzodiorite, and quartz-monzonite to syenogranite and monzogranite (Amini et al., 2001; Azizi et al., 2009; Nabatian et al., 2014a, 2016) and have metaluminous, high-K calc-alkaline (shoshonitic) and I-type geochemical characteristics (Irannezhadi et al., 2007; Azizi et al., 2009; Nabatian et al., 2014a, 2016). Contact metamorphism surrounding these intrusions is weak. They were emplaced mostly along favorable structures, such as faults and fold axes. Zircon U–Pb dating by Nabatian et al. (2014a, 2016) and Aghazadeh et al. (2015) gave an age of ~40 to 36 Ma for the emplacement of the intrusions at THMB.

The host rocks at Aliabad-Khanchy consist of Eocene volcanic and volcaniclastic rocks that were intruded by late Eocene quartz-monzonite to quartz-monzogabbro intrusions (Figs. 2 and 3). Volcanic rocks are mostly andesite with local olivine basalt lava flows. Andesitic lava flows with porphyritic texture consist predominantly of distinctive zoned phenocrysts of generally chlorite-epidote altered plagioclase and hornblende with accessory apatite, opaque and rare small zircon crystals. The basalts consist of olivine, plagioclase, and clinopyroxene phenocrysts with rare opaque minerals set in an intersertal and fine-grained groundmass. The volcaniclastic sequence is largely composed of tuff (i.e., crystal tuff, crystal lithic tuff, lithic crystal tuff, ash tuff, tuff breccia, pumiceous tuff and welded tuff),

sandy tuff and tuffaceous sandstone, up to 2000 m in thickness (Fig. 3). Andesite-basaltic andesite lava flows occur at the top of the volcaniclastic sequence (Fig. 2). Lavas and tuffs are intercalated with sandstone, siltstone and shale. The plutonic bodies (including Aliabad and Khanchy intrusions, Fig. 2) have sharp contacts with the volcanic and volcaniclastic rocks and contain few mafic microgranular enclaves. The intrusions range in composition from quartz-monzonite to quartz-monzogabbro and show similar textures and mineral assemblages. These intrusions are mainly coarse- to medium-grained rocks with porphyritic and granular textures; ophitic, subophitic and seriate textures are locally observed. They consist essentially of large phenocrysts of idiomorphic plagioclase (up to 5 cm), clinopyroxene, quartz, K-feldspar, and hornblende, with accessory apatite, biotite, opaque minerals, and zircon. The plutonic rocks are mainly calc-alkaline in composition (Saeedi et al., 2017). The host Eocene volcaniclastic rocks are locally metamorphosed to albite-epidote hornfels facies near contact intrusions.

3. Geological characteristics of the deposit

3.1. Characteristics of the mineralized veins

The Aliabad-Khanchy deposit consists of four epithermal Cu-bearing brecciated quartz veins that occupy N40E-trending faults in the Eocene volcanic (andesitic lavas) and volcaniclastic (crystal tuff, lithic crystal tuff) rocks (Figs. 2 and 4). Stockwork quartz veinlets are focused around larger veins and in zones of structural intersection. The veins display similar morphological and textural characteristics, and have regular sharp contact with host rocks, indicating that they formed by open-space filling. Base metal grades decrease gradually from the main quartz veins through stockwork quartz veinlets to argillic-altered wall-rock. The Aliabad veins (Fig. 4A-C) reach up to 600 m in length and average 1.5 m in width, reaching a maximum of 3 m. They generally dip 60 to 70° NW with a known down-dip extension of about 100 m. The Khanchy veins (Fig. 4D-E) have a strike length of 150 m, an average 1 m width, reach a maximum of 2 m and range in dip from 55 to 65° NW with a down-dip extension of about 50 m. The veins are dominated by fine- to coarse-grained quartz crystals that locally reach 2 cm in size. Vug infill and comb textures have been observed in some samples; faint crustiform banding occurs locally in the veins. Chalcopyrite content in the veins and in adjacent wall-rock commonly exceeds 5%. The veins range up to 2.2% Cu, and have an average grade of 8 g/t Ag.

3.2. Mineralization stages and wall-rock alteration

On the basis of the mineral assemblages, ore textures and crosscutting relationships of ore veins, the ore-forming process at Aliabad-Khanchy can be divided into five stages (Table 1). Stage 1 is a pre-ore stage

and is represented by zones of argillic alteration with minor disseminated and locally quartz-chalcopyrite-pyrite veinlets in andesitic lavas and lithic crystal tuffs. Clasts of this stage and associated wall-rock alteration have been recognized in the stage 2 breccias (Fig. 5A, B). Stage 2 is the most abundant, widespread, and economically important mineralization stage at Aliabad-Khanchy. This stage is characterized by 1.5 cm wide colloform/crustiform banded quartz veins and breccias that contain variable amounts of pyrite, and chalcopyrite (Fig. 5C, D). The veins are dominated by fine- to coarse-grained (up to 2 mm) quartz crystals with well-developed growth zones, comb and vug infill textures. Stage 2 veins are usually cut by stages 3, 4 and/or 5 (Fig. 5E, F). Stage 3 is represented by sets of 2 mm wide quartz veinlets that are, in turn, cut by stage 4 quartz-hematite veins and veinlets (Fig. 5E). No sulfide minerals are recognized in stage 3. Quartz typically occurs as fine-grained chalcedony with medium-grained crystals in vugs. Stage 4 is marked by 2 cm wide hematite-quartz veins and veinlets (Fig. 5F) that formed during the late stages of hydrothermal activity. Stage 5 is dominated by chlorite as veins, veinlets, and vug infill (Fig. 5G, H).

Wall-rock alteration is mainly developed along and in the vicinity of mineralized fracture zones. Alteration was recognized by variations in color, grain size, mineralogy, hardness, and style of weathering, as well as by thin section study and whole-rock geochemistry. Altered rocks are enriched in Si, Cu, Pb, Zn, Ag, V, Sr, Ta, Ba, Rb, and REE, and depleted in Na, K, Sc, and Ca (Mokhtari et al., 2016). The main wall-rock alteration types at Aliabad-Khanchy are silicification, as well as chlorite, argillic and propylitic alteration; silicification is dominant. Silica, chlorite and argillic alteration mainly occur within the mineralized zones, whereas propylitic alteration affects the wall-rock, thereby showing a clear zoning. Overall, ore grades increase gradually with increasing intensities of wall-rock alteration.

Silicification occurs next to mineralized veins and is associated with breccia cements and stockwork (up to 2 cm width) quartz veins (Fig. 6A, B). Copper mineralization is mostly in zones where silicification is most intense. Chlorite alteration usually shows a spatial relationship with zones of silicification. It occurs as vug infill and as 1 mm wide chlorite veinlets (Fig. 6C). Argillic alteration zones, with a width of about 2 m, are strongly fracture controlled and form envelopes around the quartz veins. It consists of a large quantity of sericite, illite, and minor quartz minerals (Fig. 6D). Propylitic alteration is the most distal type of alteration and is dominated by sericite, chlorite, calcite, epidote, and subordinate quartz. This alteration is typically weak to moderate intensity and generally is not texturally destructive. Plagioclase is partially to totally replaced by sericite, chlorite and calcite; pyroxene is partially to completely replaced by epidote, calcite and chlorite (Fig. 6E, F). Small amounts of quartz are present in the groundmass. Supergene

alteration is commonly focused along joints, fractures and faults. This alteration is characterized by iron oxides-hydroxides and copper carbonates, such as goethite, and malachite and azurite.

3.3. Ore mineralogy and paragenetic sequence

The hypogene ore assemblage of the Aliabad-Khanchy deposit consists of chalcopyrite (>50 vol. %), pyrite (≤15 vol. %), and hematite (≤10 vol. %) with supergene malachite, azurite, covellite, digenite and goethite. The ore minerals occur as disseminations, veinlets, and massive accumulations within veins and cements in hydrothermal breccias.

Chalcopyrite is the main ore mineral in the deposit. It typically occurs as disseminated, coarse-grained subhedral to anhedral crystals (up to 2 cm in size), or as massive aggregates in veins and in the breccia cement. In the main part of the ore zones, chalcopyrite is replaced by goethite and covellite; locally islands of relict chalcopyrite are observed (Fig. 7A, B). Pyrite is mainly disseminated, fine- to coarse-grained subhedral to anhedral crystals that range from 100 μm to 1 mm in diameter and are usually replaced by goethite (Fig. 7C). Pyrite is generally irregularly distributed in the ores, in sparse disseminated crystals, in scattered veinlets, veins or irregular aggregates with chalcopyrite. Hematite is an accessory mineral that forms bladed euhedral to subhedral crystals (specularite) with 0.5 mm to 1 cm long (Fig. 7D). It is mainly associated with quartz in stage 4 veins. Malachite occurs as vein-veinlets and vug infill. It usually fills open spaces interstitial to chalcopyrite, quartz, and chlorite (Fig. 7E).

Gangue minerals are mainly quartz and chlorite. Quartz is the most important gangue mineral. At least two quartz generations are recognized. The first one consists of crystalline quartz that is cemented or cut by microcrystalline quartz (Fig. 7E). Early quartz usually shows comb and vug infill textures (Fig. 7F). In some parts of the ore zones, cockade, colloform, and crustiform textures are observed in quartz breccia cements (Fig. 7G, H). Chlorite occurs in 1 mm wide veinlets, and also fills open spaces of quartz-sulfide breccia cement of stage 2. Chlorite is green to brown in tin section and locally shows spheroidal textures.

The mineral paragenesis of the vein and breccia cements can be subdivided into pre-ore, ore stage I, ore stage II and supergene stages (Fig. 8). The pre-ore stage is represented by minor chalcopyrite, pyrite and quartz along with sericite. Ore stage I is characterized by deposition of fine- to coarse-grained quartz, pyrite, and major chalcopyrite. Sulfide-bearing quartz veins commonly exhibit colloform/crustiform banding, cockade, as well as comb and vug infill textures. Ore stage II is characterized by deposition of microcrystalline quartz, hematite and chlorite. The alteration assemblage accompanying pre-ore stage and

ore stages I and II is quartz, sericite and illite whereas chlorite formed in the later part of ore stage II. The supergene mineral assemblage consists of malachite, azurite, covellite, digenite, and goethite.

4. Fluid inclusion studies

4.1. Sampling and analytical methods

Doubly polished plates (~150 µm thick) were prepared from 20 samples taken from outcrops for fluid inclusion studies. Quartz crystals are usually fine- to medium-grained and trapped few fluid inclusions that can be studied. This is a common feature for epithermal deposits (e.g., Bodnar et al., 1985a; Yilmaz et al., 2010). Therefore, only 5 of 20 sections had inclusions suitable for microthermometric study. Most of the fluid inclusions were trapped in coarse-grained quartz from colloform/crustiform bands of stage 2, and fewer in coarse-grained quartz of the quartz-hematite veins (stage 4). Due to small size, no workable fluid inclusions were found in microcrystalline quartz of stage 3, and inclusions were too small for microthermometry.

Fluid inclusion data represent measurements along individual planes or in groups of inclusions, i.e., fluid inclusion assemblages (Goldstein, 2003), having constant vapor to liquid ratios and that yielded consistent data. Homogenization (T_h) and ice-melting ($T_{m\text{-}ice}$) temperatures were obtained for 50 fluid inclusions representing 10 fluid inclusion assemblages in the 5 samples. Microthermometric studies were performed using a Linkam THMSG-600 heating–freezing stage (–196° to +600°C) attached to a ZEISS microscope in the fluid inclusion laboratory of Iranian Mineral Processing Research Center (IMPRC), Tehran, Iran. Calibrations were performed using cesium nitrate (melting point of +414ºC), n-Hexane (freezing point of –94.3ºC) and synthetic fluid inclusion standards. The heating rate was 5-10ºC/min at higher temperatures (>100°C), with a reproducibility of ±1°C, but was reduced to 0.1-0.5 ºC/min near phase transformation, with a reproducibility of ±0.1°C. Salinities of liquid-rich fluid inclusions were calculated from the measured last ice-melting temperatures using the equation of Hall et al. (1988). For the H_2O-NaCl-$CaCl_2$ system, salinities were calculated as NaCl (wt.%) and $CaCl_2$ (wt.%) equivalents, for which the final melting temperatures of ice and hydrohalite were needed (after Steele-MacInnis et al., 2011). The identity of the species in solution was determined from eutectic temperatures (Shepherd et al., 1985; Prokofiev et al., 2010). The interpretation of microthermometric data (composition, densities, and pressures) was performed using the software package FLUIDS (Bakker, 2003). Equations of Zhang and Frantz (1987) were used for aqueous fluids.

4.2. Petrography and fluid inclusion types

Fluid inclusions were classified as primary, secondary, and pseudosecondary using the criteria of Roedder (1984) and Goldstein (2003). Most fluid inclusions studied were primary and pseudosecondary, distributed in groups or isolated, locally in internal fractures of quartz. Inclusions ranged from 5 to 20 μm in elliptical, negative, irregular, triangular, and rounded shapes. Secondary inclusions are present, mainly in healed microfractures that extend across quartz crystals.

Four types of fluid inclusions were recognized in quartz associated with the ore according to their phase-transformations (Fig. 9): (1) Liquid-rich two-phase (LV) inclusions: liquid-phase aqueous solution and vapor bubble are both present at room temperature, with vapor phase less than 50 vol.% (mostly 10 to 35 vol.%) (Fig. 9A, D). When heated, the vapor phase disappeared and homogenized to liquid. None of the LV inclusions contain daughter minerals, and upon cooling (< –100°C), no clathrate was observed, which rules out the presence of CO_2; (2) Vapor-rich, two-phase (VL) inclusions: a liquid phase and vapor bubble are visible at room temperature, but the vapor phase is >50% in volume (usually >70 vol.%) (Fig. 9C, D). This kind of fluid inclusion generally coexists with two-phase, LV aqueous inclusions, but such inclusions are relatively rare. VL inclusions homogenized to vapor on heating; (3) Liquid-phase (L) aqueous inclusions: only one phase of liquid solution is visible at room temperature, without any vapor phase (Fig. 9A, D); (4) Vapor-phase (V) inclusions: only one phase of vapor bubble is present without any visible liquid solution at room temperature (Fig. 9B). Neither liquid CO_2 nor CH_4 was observed during the freezing experiments.

Among the four types of fluid inclusions, the first two are dominant; LV dominates over the VL with about 70 vol.% of the total inclusion population. Quartz in different hydrothermal ore stages contains different combinations of fluid inclusions. Stage 2 and 3 quartz contains fluid inclusion assemblages of LV, VL, L and/or V types; whereas stage 4 quartz contains only two-phase fluid inclusion assemblages. Coexistence of the four types of fluid inclusions in the Aliabad-Khanchy ores indicates that the fluid inclusions captured heterogeneous fluids and suggests that phase separation (i.e., boiling) occurred during mineralization.

4.3. Microthermometry

Microthermometric analyses were conducted on primary LV fluid inclusions. Most of the LV aqueous inclusions froze at temperatures between –70° and –90°C. Upon heating, first ice-melting (T_e) and final ice-melting temperatures ($T_{m\text{-}ice}$) were recorded for most of the aqueous inclusions, whereas only few hydrohalite melting temperatures ($T_{m\text{-}hh}$) were recorded in stage 2 quartz due to the metastable behavior of this phase. In inclusions where melting temperatures of both ice and hydrohalite were measured, the fluid

compositions were determined using the approach of Steele-MacInnis et al. (2011). During the freezing–heating process, it is very difficult to observe the final ice-melting for VL inclusions; hence the $T_{m\text{-}ice}$ values could not be measured. In addition, because of decrepitation, the homogenization temperatures of VL inclusions with <10 vol.% liquid could not generally be determined. However, two isolated VL inclusions were measured and their salinities and homogenization temperatures are similar to those of the adjacent LV inclusions.

To avoid problems associated with inclusion necking, heating-freezing measurements were made only on inclusions with uniform L:V ratios. Because boiling is indicated by coexisting LV and VL inclusions, the homogenization temperatures require no pressure corrections. The microthermometric data are summarized in Table 2 and plotted in Figure 10.

First ice-melting and final ice-melting temperatures of LV inclusions in fluid inclusion assemblages of stage 2 quartz veins range from –45° to –52°C and–3° to –16.4°C, respectively (Table 2, Fig. 10A). This is consistent with the presence of mixed chloride species such as NaCl, KCl, $CaCl_2$, $MgCl_2$, and $FeCl_2$ in the trapped fluids (e.g., Roedder, 1984; Shepherd et al., 1985; Van Den Kerkhof and Hein, 2001; Prokofiev et al., 2010). Clathrate was never observed in LV inclusions upon cooling, indicating that these inclusions contain negligible carbon species (e.g., Rosso and Bodnar, 1995; Ouyang et al., 2014). Hydrohalite melting ($T_{m\text{-}hh}$) in the stage 2 quartz-hosted LV inclusions was between –23° and –32°C. For the H_2O–NaCl–$CaCl_2$ system, these results indicate bulk salinities from 8.3 to 24.5 wt.% NaCl+$CaCl_2$ equiv., with NaCl contents of 5.3 to 14 wt.%, $CaCl_2$ content from 3 to 18.3 wt.%, and NaCl/(NaCl+$CaCl_2$) ratios in the range of 0.2 to 1 (Fig. 10B). The average homogenization temperature (T_h) of LV inclusions in fluid inclusion assemblages of stage 2 quartz (homogenize to the liquid state) ranges from 190° to 290°C, with the majority of T_h varying from 230° to 270°C (Table 2, Fig. 10C). Bulk salinities of fluid inclusions range from 5.1 to 19.7 (with a mode of 12.4) wt.% NaCl+$CaCl_2$ equiv. (Table 2, Fig. 10D). The bulk density of such fluids is from 0.84 to 1 g/cm^3 (Fig. 11). The $T_{m\text{-}hh}$ results are shown in the H_2O–NaCl–$CaCl_2$ ternary diagram in Figure 12.

All LV inclusions in stage 4 quartz also homogenized to the liquid state. The average T_h of LV inclusions in fluid inclusion assemblages of this stage ranges from 150° to 230°C; with the majority of T_h varying from 190° to 220°C (Table 2, Fig. 10C). For these inclusions, T_e values were from –30° to –35°C, indicating the presence of Na, K, and Ca chlorides (Shepherd et al., 1985; Prokofiev et al., 2010). The $T_{m\text{-}ice}$ values are in the range of –3° to –8.5°C (Fig. 10A). The calculated bulk salinity is 5.1 to 12.4 (with a mode of 6.6) wt.% NaCl equiv. (Table 2, Fig. 10D) and the bulk density is 0.91 to 0.98 g/cm^3 (Fig. 11).

5. Stable isotopes

5.1. Sampling and analytical methods

Samples were collected from both the Aliabad and Khanchy mineralized brecciated quartz veins. Samples were selected to represent the five-stage evolution of the mineralization. Mineral aggregates were removed from the samples using tweezers and then were crushed and sieved to 0.1–0.5 mm. After panning, clean mineral grains (quartz and sulfides) were then handpicked under a binocular microscope. As a further purification step, quartz separates were washed in hot (ca. 90°C) 6 M HCl several times with a final rinse in hot (ca. 90°C) Milli Q water to remove ''soluble'' impurities adhering to grain surfaces (e.g., iron oxides). This was followed by ultrasonic cleaning in cold Milli Q water for 5 minutes to remove ''insoluble'' surface impurities (e.g., clay minerals). The samples were then dried in an oven at 80°C. For sulfides, approximately 10 to 50 mg were leached in acetone to remove surface contamination and then washed in distilled water and dried at 60°C. Mineral separates were at least 99% pure.

Six chalcopyrite samples from stage 2 quartz veins were analyzed for sulfur isotopes. Sulfur isotopes were measured at the laboratories of the USGS Southwest Isotope Research Laboratory in Denver, USA. Sulfides were combined with V_2O_5 and combusted in a Thermo Scientific Flash 2000 Elemental Analyzer; the resulting SO_2 flowed directly into a Thermo Finnigan Delta Plus XP™ continuous flow mass spectrometer for the sulfur isotope measurement (Johnson et al., in press); with a precision of ±0.5‰ (2σ). Analytical precision was based on replicate analyses. Calibration was based on the internationally distributed standards NBS123 +17.44‰ and IAEA-S-3 –32.55 ± 0.12‰ (Coplen et al., 2002). The $\delta^{34}S$ values are reported relative to the Vienna Cañon Diablo Troilite (VCDT) standard.

Oxygen isotopic analysis was conducted on 2 handpicked quartz mineral separates from stage 2 and 4 veins and breccia cement. Oxygen isotope analyses were performed at the National Isotope Centre, New Zealand, using a laser-based extraction technique with BrF_5 as the reagent, and isotope analyses were performed on molecular oxygen, modified after the technique of Sharp (1990). Samples were heated using CO_2-laser fluorination, and the isotope analyses were performed using a Europa Geo 20-20 stable isotope ratio mass spectrometer in dual inlet mode. Samples and standards were heated overnight to 150°C prior to loading into the vacuum extraction line. These were then evacuated for ~6 hours. Blank BrF_5 runs were carried out until yield was less than 0.2 μmoles oxygen. Results are reported in $\delta^{18}O$ notation relative to Vienna-Standard Mean Ocean Water (V-SMOW) using values of +9.6‰ and +5.8‰ for standards NBS-28 and UWG-2 Garnet, respectively. The reproducibility was below 0.15‰.

The $\delta^{34}S$ values of reduced sulfur (H_2S) in equilibrium with the chalcopyrite were calculated using the fractionation equation of Li and Liu (2006), whereas oxygen isotopic compositions of hydrothermal waters in equilibrium with quartz were calculated using the fractionation equation of Méheut et al. (2007). The isotopic compositions were calculated using the mean value of the homogenization temperatures.

5.2. Results

The isotopic compositions of oxygen and sulfur for the Aliabad-Khanchy samples are listed in Table 3. The $\delta^{18}O_{quartz}$ value of quartz in stage 2 veins is +13‰, and that for quartz in stage 4 quartz-hematite veins is +13.6‰. For the average temperature of fluid inclusion assemblages, the fluids of stage 2 quartz have a $\delta^{18}O_{water}$ value of about +3.6‰ (Table 3). The calculated $\delta^{18}O_{water}$ value of stage 4 quartz-hematite veins is +0.8‰ (Table 3), which is lower than $\delta^{18}O_{water}$ of stage 2 quartz. The $\delta^{34}S_{sulfide}$ values of chalcopyrite in stage 2 veins range from –7.9 to –4.8‰ (Table 3). The average calculated $\delta^{34}S$ values of hydrothermal fluid in equilibrium with the sulfides range from –8.1 to –5.0‰ (Table 3).

6. Discussion

6.1. Ore-forming fluids and sulfur sources

The lack of hydrogen isotope values, as well as lack of knowledge of the isotopic composition of meteoric fluids in THMB at the time of mineralization, prevents definitive identification of fluid sources (e.g., Mehrabi et al., 2016). Studies of fluid-mineral isotopic equilibrium in geothermal systems have shown that quartz is very resistant to isotopic exchange and preserves its original isotopic signature (Clayton et al., 1968; Taylor, 1968; Blattner, 1975; Clayton and Steiner, 1975; Fifarek and Rye, 2005; Corral et al., 2017). If the hydrothermal fluids had uniform oxygen isotopic composition, the increase in $\delta^{18}O$ would reflect decreasing temperatures of mineral precipitation, which is in agreement with the decrease in the homogenization temperatures obtained from fluid inclusions.

Oxygen isotope values and estimated oxygen isotope composition of the ore fluids for stage 2 quartz (Table 3) are similar to those of epithermal deposits in volcano-plutonic environments (e.g., Vallance et al., 2003, 2004), suggesting that the fluids were dominantly magmatic, although one can never fully rule out water–rock reaction between meteoric water and surrounding altered volcanic wall-rocks (e.g., Field and Fifarek, 1985; Hedenquist and Lowenstern, 1994; Simmons, 1995; Zhai et al., 2009; Zhang et al., 2013). The stage 4 fluids are more depleted in ^{18}O suggesting a significant input of meteoric water into the fluid system, which is a characteristic of other epithermal deposits (e.g., Rye, 1993; Hedenquist and Lowenstern, 1994; Wang et al., 1999; Cooke and McPhail, 2001).

Estimates of fluid salinities show that the ore-forming fluids were diluted from early to late, which are in accord with the oxygen isotope evidence for dilution by meteoric water. Salinities of the LV fluid inclusions in quartz of stages 2 and 4 are as high as 19.7 wt.% NaCl+$CaCl_2$ equiv., and up to 12.4 wt.% NaCl equiv., respectively. This indicates that the initial ore-fluids were likely sourced from a magmatic system progressively diluted by meteoric water during later ore stages. This interpretation is similar to interpretations of other magmatic-hydrothermal systems, such as those in Canada, Mexico and Mongolia (e.g., Thiersch et al., 1997; Camprubi and Albinson, 2007; Zhai et al., 2013).

$\delta^{34}S$ values of about 0‰ are usually interpreted as the result of magmatic sulfur escaping from a crystallizing magma (Ohmoto and Rye, 1979; Faure, 1986; Rye, 1993; Kouzmanov and Ramboz, 2003; Moritz et al., 2003). The sulfur values for the Aliabad-Khanchy deposit are significantly below 0‰. Such low $\delta^{34}S_{sulfide}$ values are consistent with either a magmatic source of sulfur under conditions sufficiently oxidizing to stabilize SO_4^{2-} or a sedimentary component (Ohmoto and Rye, 1979; Kouzmanov and Ramboz, 2003; Moritz et al., 2003; Yilmaz et al., 2010). A vast amount of $\delta^{34}S_{sulfide}$ data ranging from 3 to –10‰ is reported for Andean epithermal/magmatic systems (e.g., Carrillo-Rousa et al., 2008). Considering the volcanic nature of the host rocks at the Aliabad-Khanchy, it is more likely that the sulfur in the ore fluids originated by scavenging from volcanic host rocks or, less probably, from a magma driving the system (e.g., Cooke and Simmons, 2000; Yilmaz et al., 2010).

6.2. Evolution of ore-forming fluids

A fluid evolution diagram for the Aliabad-Khanchy deposit is shown in Figure 13 on a T_h-salinity plot with boundaries of magmatic and meteoric waters (Lattanzi, 1991; Hedenquist and Arribas, 1998; Naden et al., 2005). The evolutionary trend is interpreted to be the product of mixing between a saline, moderate to high temperature fluid (290°C, 19.7 wt.% NaCl+$CaCl_2$ equiv.) and a dilute, cooler fluid of meteoric origin (e.g., Richards et al., 1997; Yilmaz et al., 2010; Canet et al., 2011). Conversely, the trend could be the result of boiling (e.g., Hedenquist and Henley, 1985; Wilkinson, 2001; Klemm et al., 2007; Canet et al., 2011; Ouyang et al., 2014). Inclusions of trapped boiling fluids commonly show the characteristics of high-density brine, low-density vapor and intermediate-density solution that occur in the same regions of the same samples (e.g. Ramboz et al., 1982; Simmons and Browne, 2000; Rusk et al., 2008; Ouyang et al., 2014). This explanation has been used to account for other epithermal systems such as those in Japan, New Zealand and Mexico (e.g., Sherlock et al., 1995; Scott and Watanabe, 1998; Simpson et al., 2001; Camprubi and Albinson, 2007; Kouhestani et al., 2015).

Analyses of fluid inclusions of the Aliabad-Khanchy deposit revealed that the fluids can be divided into two groups: (1) moderate to high temperature and salinity with average of ca. 245°C and 12.4 wt.% NaCl+$CaCl_2$ equiv. (stage 2), and (2) slightly lower temperature (ca. 185°C) with much lower salinities of 6.6 wt.% NaCl equiv. (stage 4). Variations in the salinity content of fluids can be explained in terms of multiple fluid sources, fluid boiling and fluid mixing. On a fluid evolution diagram (Fig. 13), fluid salinity shows a positive correlation with the homogenization temperatures implying that there is mixing between hydrothermal solutions with different sources and compositions, for example, magmatic fluid and meteoric water, during mineralization at Aliabad-Khanchy. Previous studies have shown that homogenization temperature and fluid salinity show positive correlations during the process of fluid mixing, whereas these data show negative correlation trends during fluid boiling (e.g., Shepherd et al., 1985; Zhai et al., 2009; Zhai et al., 2013).

The oxygen isotope data also suggest that more than one fluid existed during the formation of the Aliabad-Khanchy deposit. The sulfur isotope compositions of sulfides imply that metallogenic materials at Aliabad-Khanchy ultimately originated from magmatic activity. Quartz oxygen isotope data indicate that the source of hydrothermal fluids was dominantly magmatic waters. These data also indicate that in addition to the contribution of magmatic fluids, meteoric water played a role in the mineralization processes. Based on these arguments, it is suggested that fluid mixing occurred during the fluid evolution, as well as fluid boiling, and it seems clear for the Aliabad-Khanchy deposit that fluid mixing played a more important role than fluid boiling.

6.3. Trapping pressure and mineralization depth

Fluid inclusion petrography for the Aliabad-Khanchy deposit shows that the LV and VL inclusions are usually within same quartz growth zones during precipitation of ore veins (Fig. 9). This is usually interpreted as a consequence of trapping of a heterogeneous boiling fluid (e.g., White and Hedenquist, 1995; Thiersch et al., 1997; Ronacher et al., 2000; Simmons et al., 2005; Prokofiev et al., 2010; Ouyang et al., 2014). However, this can also occur through sequential trapping of different fluids at different times by necking down or by leakage (e.g., Ramboz et al., 1982; Rusk et al., 2008). Important evidence for trapping of boiling fluids is that the inclusions must be trapped contemporaneously (Ramboz et al., 1982; Ouyang et al., 2014). The opposite modes of homogenization of LV and VL fluids (LV→L and VL→V) within the same range of temperatures suggest that boiling of the ore fluid could have occurred during vein formation at Aliabad-Khanchy. Boiling is also consistent with the presence of colloform and chalcedonic quartz (e.g., White and Hedenquist, 1990; Hedenquist et al., 2000; Kouhestani et al., 2015,

2017; Mehrabi et al., 2016) within the ore zones. Deposition of chalcedonic quartz points to rapid deposition of SiO_2, possibly due to the rapid cooling accompanying boiling, and caused by the loss of heat carried away by water vapor (e.g., Thiersch et al., 1997). Furthermore, the ore veins in the Aliabad-Khanchy commonly have regular, sharp contacts with their volcanic host rocks. These characteristics may suggest that the veins/veinlets formed by open-space filling under a hydrostatic pressure (e.g., Hedenquist et al., 1998; Liu et al., 2014; Ouyang et al., 2014; Siahcheshm et al., 2014). Indeed, the presence of hydrothermal breccias in stage 2 veins with base metal mineralization is evidence for periods of sharp pressure drops. These may have led to at least intermittent boiling in a hydrothermal system.

Recognition of fluid inclusions trapped under boiling conditions is valuable for P-T estimations, because pressure correction is not needed and the homogenization temperature is equal to the trapping temperature (e.g., Roedder and Bodnar, 1980; Simeone and Simmons, 1999; Ouyang et al., 2014). Following Albinson (1988) and Hedenquist et al. (1998), the highest temperatures of the LV inclusions are used for pressure and depth estimation for the Aliabad-Khanchy deposit. The trapping pressures of these inclusions are estimated using the experimental data of Bodnar et al. (1985b), Haas (1971), and Urusova (1975), as is shown in Figure 14. The calculated entrapment pressures of fluid inclusions from stage 2 through stage 4 quartz at Aliabad-Khanchy range from about 79 to 50 bar, equivalent to hydrostatic depths of about 790 to 500 m below the paleowater table. The calculated depth range is consistent with the estimated mineralization depths of the epithermal deposits worldwide (Simmons et al., 2005; Pirajno, 2009).

6.4. Mineralization model and genetic type

The Aliabad-Khanchy base metal deposit is an epithermal deposit as described by White and Hedenquist (1990), Hedenquist et al. (2000), Sillitoe and Hedenquist (2003), Einaudi et al. (2003), Moritz et al. (2003), Gemmell (2004) and Simmons et al. (2005). This is evidenced by the recognition of: (1) epithermal textures, such as hydrothermal veins and breccias with vug infill, comb, cockade, colloform, and crustiform textures; and (2) hydrothermal alteration represented by sericite, illite, epidote, calcite, and chlorite. In addition, the medium- to high-temperature, moderate-salinity, and low-density of ore fluids at Aliabad-Khanchy are typical of epithermal precious and base metal systems noted in the THMB of northwestern Iran (e.g., Mehrabi et al. 2010, 2016; Kouhestani et al., 2017) and elsewhere (e.g., Albinson et al., 2001; John, 2001; Yilmaz et al., 2010; Sabeva et al., 2017). The general absence of adularia, alunite and carbonates in mineralized quartz veins, and the absence of vuggy quartz, lattice-textured and bladed calcite as well as advanced argillic alteration in the Aliabad-Khanchy deposit distinguish the Aliabad-Khanchy base metal veins from low- and high-sulfidation epithermal deposits. Such a mineralization style

was termed intermediate-sulfidation by Hedenquist et al. (2000). In addition, paleodepths of ~500 m are characteristic of silver- and base metal-rich of epithermal systems of the intermediate-sulfidation category (Hedenquist et al., 2000; Albinson et al., 2001).

Cooling, mixing, boiling and water–rock reaction are the main factors that can promote the precipitation of precious and base metals from an ore fluid in the epithermal environment (e.g., Giggenbach and Stewart, 1982; Heald et al., 1987; Hayba, 1997; Hedenquist et al., 2000; Federico et al., 2002; Zhai et al., 2009; Corral et al., 2017). Boiling is considered to be the main factor leading to deposition of precious metals in many epithermal deposits (e.g., Izawa et al., 1990; Simon et al., 1999; Simmons et al., 2000; Faure et al., 2002; John et al., 2003), whereas the dilution and/or cooling resulting from fluid mixing are key mechanisms for base metal precipitation (e.g., Spycher and Reed, 1989; Yilmaz et al., 2007, 2010; Kouhestani et al., 2015, 2017).

Oxygen isotope data for quartz and fluid inclusions from mineralized quartz veins indicate that at least two fluids existed during the formation of the Aliabad-Khanchy deposit. The early ore-forming fluids had relatively higher temperature and salinity, and were dominantly magmatic in origin (Fig. 15). Copper was likely transported by chloride complexes, and due to low sulfur fugacity of the fluids, most of Cu remained in solution until there was an increase in sulfur fugacity during stage 2. It is also assumed that chlorine was magmatic in origin because of the lack of evaporites and connate brines in the region (e.g., Mehrabi et al., 2016; Kouhestani et al., 2017). The occurrence of colloform and chalcedonic quartz along with fluid inclusion data indicates that boiling was one of the processes affecting hydrothermal fluids. It is thus probable that the deposition of chalcopyrite was caused by destabilization of chloride complexes as a result of partitioning of H_2S into the vapor phase associated with boiling (e.g., Drummond and Ohmoto, 1985; Henley, 1985). This process led to decrease in sulfur fugacity and increase in pH, both enhanced chalcopyrite deposition (e.g., Thiersch et al., 1997).

Magmatic ore-forming fluids ascended along favorable structures and fracture zones and reacted with wall-rocks, changing the physicochemical conditions and isotopic compositions of the fluids. It seems that the fluids have ascended to a sufficiently shallow depth to allow efficient fluid mixing with meteoric waters (Fig. 15; e.g., Cooke and McPhail, 2001; Fan et al., 2011; Gu et al., 2011). Through the reaction of mineralizing magmatic fluids with wall-rocks and heat recharge by magma, fluids could have extracted significant amounts of metallogenic materials from host rocks. Fluid mixing changed the conditions of the ore-forming fluid system, destroying the chemical equilibrium of solutions and initiating important chemical reactions, ultimately resulting in the precipitation of copper from solution during the

mineralization process. Consequently, the fluid mixing hypothesis is the main mechanism that could explain the deposition of chalcopyrite in stage 2 quartz veins (e.g., Henley et al., 1984; Drummond and Ohmoto, 1985; Henley, 1985; Kouhestani et al., 2015, 2017; Mehrabi et al., 2016). The relatively lower temperature and salinity of stage 4 quartz-hosted fluid inclusions suggest that the ore-forming fluids during this stage are predominantly meteoric waters that have reacted with the host rocks (e.g., Giggenbach et al., 1990; Giggenbach, 1992; Cooke and Simmons, 2000). Significant increase in the oxygenated meteoric water component would eventually increase oxygen fugacity, which agrees with the presence of specular hematite in stage 4 quartz veins. This interpretation is consistent with models for the formation of other epithermal precious and base metal deposits in the THMB, such as those described by Mehrabi et al. (2010, 2016), Hosseinzadeh et al. (2016) and Kouhestani et al. (2017).

7. Exploration implications

During the early to middle Eocene, intense magmatic activity in the THMB resulted in the deposition of up to a 2000 m thick volcaniclastic succession. Northwest- and northeast-striking normal faults formed during this magmatism. Late Eocene high-K to shoshonitic granitoid stocks that exhibit a close temporal and spatial relationship with epithermal mineralization were emplaced along favorable structures, such as faults, and fold axes.

Oxygen and sulfur isotopic signatures along with fluid inclusion data indicate that the Aliabad-Khanchy deposit is the product of a magmatic-hydrothermal system. The style of the wall-rock alterations and the patterns related to mineralization in the Aliabad-Khanchy deposit are similar to those of other precious and base metal deposits present in the THMB, i.e., Chodarchay, Gulojeh, Khalyfehlou, Lohneh, Rashtabad, Jalilabad, and Aqkand. Considering the close temporal and spatial association of the granitoid intrusions with epithermal mineralization, it may be inferred that these intrusions are genetically related to the epithermal mineralization in the THMB. Furthermore, the location of the hydrothermal alteration and mineralization zones in dilational sites along the fault systems at Aliabad-Khanchy and other epithermal mineralization in the THMB suggests that the fault structures provided a focus for upward migration of magmatic fluids (e.g., Yasami et al., 2017) to depths shallow enough for boiling and/or mixing with meteoric water, thereby causing precious and base metal precipitation. Investigation of fault zones within altered Eocene volcanic and volcaniclastic rocks, particularly close to granitoid intrusions, therefore has important implications for exploration targeting of epithermal ores at THMB and possibly in the other parts of the Alborz magmatic arc.

8. Conclusions

The Aliabad-Khanchy base metal deposit in THMB, northwestern Iran, is hosted by volcanic and volcaniclastic rocks of the Karaj Formation and was controlled primarily by normal faults. Fluid inclusion data and oxygen and sulfur isotope geochemistry reveal that the ore-forming fluid was sourced from dominantly magmatic water in the early stages and evolved to dominantly meteoric water in the late stage. The positive correlation between homogenization temperature and fluid salinity, combined with isotope compositions and ore deposit geology, provides evidence that fluid mixing was an important process in the evolution of the ore-forming fluids at Aliabad-Khanchy. This process resulted in cooling, breakdown of metal-Cl complexes, and reduced Cu solubility in the metal-bearing fluids. These changes were the main factors for the precipitation of chalcopyrite in the ore zones. Nevertheless, the opposite modes of homogenization of LV and VL fluids within the same range together with presence of hydrothermal breccias, colloform and chalcedonic quartz also suggests that boiling could have been important in controlling ore deposition at Aliabad-Khanchy deposit.

Mineralization at Aliabad-Khanchy is an intermediate-sulfidation type of epithermal precious and base metal system similar to other hydrothermal deposits of the THMB. These epithermal deposits have temporal, spatial, and plausible genetic links with late Eocene magmatism, and are associated with hydrothermal activity controlled by fault and fracture systems. The magmatic activity provided not only ore-forming fluids but also conduits for transport of ore-bearing fluids and structural sites for ore deposition. Thus, altered Eocene volcanic and volcaniclastic rocks, especially at the intersection of subvolcanic stocks and faults, are the most favorable locus for epithermal ore bodies at THMB.

Acknowledgments

This research was made possible by the grant of the office of vice chancellor for research and technology, University of Zanjan. We acknowledge their support. S. Aghajani (IMPRC) is thanked for carrying out fluid inclusion analyses. Appreciation is also extended to D. John for his constructive suggestions on the earlier draft of the manuscript. The manuscript has benefited from helpful comments by A. Maghsoudi, H. Mirnejad and careful editorial work by F. Pirajno. Any use of trade, firm, or product names is for descriptive purposes only and does not imply endorsement by the U.S. Government.

References

Aghanabati, A., 2004. Geology of Iran. Geol. Surv. Iran, Tehran, 606 p. (in Persian).

Aghazadeh, M., Badrzadeh, Z., Castro, A., 2015. Petrogenesis and U-Pb SHRIMP Dating of Tarom Plutons. J. Geosci. 24 (95), 3–20 (in Persian with English abstract).

Aghazadeh, M., Castro, A., Badrzadeh, Z., Vogt, K., 2011. Post-collisional polycyclic plutonism from the Zagros hinterland: The Shaivar Dagh plutonic complex, Alborz belt, Iran. Geol. Mag. 148, 980–1008.

Alavi, M., 1991. Tectonic map of the Middle East (scale 1:5,000,000): Geol. Surv. Iran.

Albinson, T.F., 1988. Geologic reconstruction of paleosurfaces in the Sombr-erete, Colorado, and Fresnillo districts, Zacatecas State, Mexico. Ecol. Geol. 83, 1647–1667.

Albinson, T., Norman, D.I., Cole, D., Chomiak, B., 2001. Controls on formation of low-sulfidation epithermal deposits in Mexico: Constraints from fluid inclusion and stable isotope data. In: Albinson, T., and Nelson, C.E., (Eds.), New Mines and Discoveries in Mexico and Central America. Econ Geol. Spec. Pub. 8, 1-32.

Amini, B., Amini, M.R., Stöcklin, J., Hirayama, K., 2001. Geological map of Tarom, Sheet no. 5763, Scale 1:100000, 1 sheet: Geol. Surv. Iran.

Asiabanha, A., Foden, J., 2012. Post-collisional transition from an extensional volcano-sedimentary basin to a continental arc in the Alborz Ranges, N-Iran. Lithos 148, 98–111.

Azizi, H., Jahangiri, A., 2008. Cretaceous subduction-related volcanism in the northern Sanandaj-Sirjan Zone, Iran. J. of Geod. 45, 178–190.

Azizi, H., Mehrabi, B., Akbarpour, A., 2009. Genesis of Tertiary magnetite-apatite deposits, southeast of Zanjan, Iran: Res. Geol. 59, 330–341.

Bakker, R.J., 2003. Package FLUIDS 1, Computer programs for analysis of fluid inclusions data and for modeling bulk fluid properties. Chem. Geol. 194, 3–23.

Blattner, P., 1975. Oxygen isotopic composition of fissure-grown quartz, adularia, and calcite from Broadlands geothermal field, New Zealand. Am. J. Sci. 275, 785–800.

Bodnar, R.J., Burnham, C.W., Sterner, S.M., 1985b. Synthetic fluid inclusions in natural quartz. III. Determination of phase equilibrium properties in the system H_2O–NaCl to 1000°C and 1500 bars. Geochim. Cosmochim. Acta 49, 1861–1873.

Bodnar, R.J., Reynolds, T.J., Kuehn, C.A., 1985a. Fluid-inclusion systematics in epithermal systems. Reviews in Economic Geology 2, 1–24.

Bouzari, F., Clark, A.H., 2006. Prograde evolution and geothermal affinities of a major porphyry copper deposit: The Cerro Colorado Hypogene Protore, I Region, Northern Chile. Econ. Geol. 101, 95–134.

Camprubí, A., Albinson, T., 2007. Epithermal deposits in Mexico: Update of current knowledge, and an empirical reclassification. Geol. Soc. Spec. Pap. 422, 377–415.

Canet, C., Franco, S.I., Prol-Ledesma, R.M., González-Partida, E., Villanueva-Estrada, R.E., 2011. A model of boiling for fluid inclusion studies: Application to the Bolaños Ag–Au–Pb–Zn epithermal deposit, Western Mexico. J. Geochem. Expl. 110, 118–125.

Carrillo-Rousa, J., Morales-Ruano, S., Morata, S., Boyce, D.A., Belmar, M., Fallick, A.E., Fenoll Hach-Ali, P.F., 2008. Mineralogy and geochemistry of El Dorado epithermal gold deposit, El Sauce district, central-northern Chile. Miner. and Pet. 92, 341–360.

Castro, A., Aghazadeh, M., Badrzadeh, Z., Chichorro, M., 2013. Late Eocene–Oligocene postcollisional monzonitic intrusions from the Alborz magmatic belt, NW Iran: An example of monzonite magma generation from a metasomatised mantle source. Lithos 180–181, 109–127.

Chen, Y.J., Pirajno, F., Li, N., Guo, D.S., Lai, Y., 2009. Isotope systematics and fluid inclusion studies of the Qiyugou breccia pipe-hosted gold deposit, Qinling Orogen, Henan province, China: Implications for ore genesis. Ore Geol. Rev. 35 (2), 245–261.

Clayton, R.N., Muffler, L.J.P., White, D.E., 1968. Oxygen isotope study of calcite and silicates of the River Ranch NO. 1 well, Salton Sea geothermal field, California. Am. J. Sci. 266, 968–979.

Clayton, R.N., Steiner, A., 1975. Oxygen isotope studies of the geothermal system at Wairakei, New Zealand. Geochim. Cosmochim. Acta 39, 1179–1186.

Cooke, D.R., McPhail, D.C., 2001. Epithermal Au–Ag–Te mineralization, Acupan, Baguio district, Philippines: Numerical simulations of mineral deposition. Econ. Geol. 96, 109–131.

Cooke, D.R., Simmons, S.F., 2000. Characteristics and genesis of epithermal gold deposits. Rev. Econ. Geol. 13, 221–244.

Coplen, T.B., Hopple, J.A., Böhlke, J.K., Peiser, H.S., Rieder, S.E., Krouse, H.R., Rosman, K.J.R., Ding, T., Vocke, Jr., R.D., Revesz, K.M., Lamberty, A., Taylor, P., De Bièvre, P., 2002. Compilation of minimum and maximum isotope ratios of selected elements in naturally occurring terrestrial materials and reagents. U.S. Geological Survey Water-Resources Investigations Report 01–4222, 98 p.

Corral, I., Cardellach, E., Corbella, M., Canals, À., Griera, A., Gómez-Gras, D., Johnson, C.A., 2017. Origin and evolution of mineralizing fluids and exploration of the Cerro Quema Au-Cu deposit (Azuero Peninsula, Panama) from a fluid inclusion and stable isotope perspective. Ore Geol. Rev. 80, 947–960.

Drummond, S.E., Ohmoto, H., 1985. Chemical evolution and mineral deposition in boiling hydrothermal systems. Econ. Geol. 80, 126–147.

Einaudi, M.T., Hedenquist, J.W., Inan, E.E., 2003. Sulfidation state of fluids in active and extinct hydrothermal systems: Transitions from porphyry to epithermal environments. In: Simmons, S.F., Graham I (Eds.), Volcanic, geothermal, and ore-forming fluids: rulers and witnesses of processes within the earth. Econ. Geol. Spec. Pub. 10, 285–313.

Esmaeli, M., Lotfi, M., Nezafati, N., 2015. Fluid inclusion and stable isotope study of the Khalyfehlou copper deposit, southeast Zanjan, Iran. Arab. J. Geosci. 8, 9625–9633.

Fan, H.R., Hu, F.F., Wilde, S.A., Yang, K.F., Jin, C.W., 2011. The Qiyugou gold-bearing breccia pipes, Xiong'ershan region, central China: Fluid-inclusion and stable-isotope evidence for an origin from magmatic fluids. Int. Geol. Rev. 53, 25–45.

Faure, G., 1986. Principles of isotope geology, 2nd edition. John Wiley and Sons, New York. 589 p.

Faure, K., Matsuhisa, Y., Metsugi, H., Mizota, C., Hayashi, S., 2002. The Hishikari Au–Ag epithermal deposit, Japan: Oxygen and hydrogen isotope evidence in determining the source of paleohydrothermal fluids. Eco. Geol. 97, 481–498.

Federico, C., Aiuppa, A., Allard, P., Bellomo, S., Jean-Baptiste, P., Parello, F., Valenza, M., 2002. Magma-derived gas influx and water–rock interactions in the volcanic aquifer of Mt. Vesuvius, Italy. Geochim. Cosmochim. Acta 66, 963–981.

Feizi, M., Ebrahimi, M., Kouhestani, H., Mokhtari, M.A.A., 2016. Geology, mineralization and geochemistry of Aqkand Cu occurrence (north of Zanjan, Tarom-Hashtjin zone). J. Econ. Geol. 8 (2), 507–524 (in Persian with extended English abstract).

Field, C.W., Fifarek, R.H., 1985. Light stable-isotope systematics in the epithermal environment. Rev. Econ. Geol. 2, 99–128.

Fifarek, R.H., Rye, R., 2005. Stable isotope geochemistry of the Pierina high-sulfidation Au-Ag deposit, Peru; influence of hydrodynamics on SO_4^{2-}-H_2S sulfur isotopic exchange in magmatic-steam and steam-heated environments. Chem. Geol. 215, 253–279.

Gemmell, J.B., 2004. Low- and intermediate-sulfidation epithermal deposits. In: Cooke, D.R., Deyell, C.L., Pongratz, J. (Eds.), 24 Carat Gold Workshop. Centre for Ore Dep. Res. Spec. Pub. 5, 57–63.

Ghasemi Siani, M., Mehrabi, B., Azizi, H., Wilkinson, C.M., Ganerod, M., 2015. Geochemistry and geochronology of the volcano-plutonic rocks associated with the Glojeh epithermal gold mineralization, NW Iran. Open Geosci. 7, 207–222.

Ghorbani, M. 2013. The economic geology of Iran: Mineral deposits and natural resources. Springer, London, 569 pp.

Giggenbach, W.F., 1992. Magma degassing and mineral deposition in hydrothermal systems along convergent plate boundaries. Econ. Geol. 87, 1927–1944.

Giggenbach, W.F., Garcia, P.N., Londono, C.A., Rodriguez, V.L., Rojas, G.N., Calvache, V.M.L., 1990. The chemistry of fumarolic vapor and thermal spring discharges from the Nevado del Ruiz volcanic–magmatic–hydrothermal system. J. Volcano. Geotherm. Res. 42, 13–39.

Giggenbach, W.F., Stewart, M.K., 1982. Processes controlling the isotopic composition of steam and water discharges from steam vents and steam-heated pools in geothermal areas. Geoth. 11, 71–80.

Goldstein, R.H., 2003. Petrographic analysis of fluid inclusions. In: Samson, I., Anderson, A., Marshall, D. (Eds.), Fluid Inclusions: Analysis and Interpretation. Min. Assoc. of Can. Short Course 32, 9–53.

Gu, L.X., Wu, C.Z., Zhang, Z.Z., Franco, P., NI, P., Chen, P.R., Xiao, X.J., 2011. Comparative study of ore-forming fluids of hydrothermal copper–gold deposits in the lower Yangtze River Valley, China. Int. Geol. Rev. 53, 477–498.

Haas, J.L., 1971. The effect of salinity on the maximum thermal gradient of a hydrothermal system at hydrostatic pressure. Econ. Geol. 66, 940–946.

Hall, D.L., Sterner, S.M., Bodnar, R.J., 1988. Freezing point depression of NaCl–KCl–H_2O solutions. Econ. Geol. 83, 197–202.

Hayba, D.O., 1997. Environment of ore deposition in the Creede mining district, San Juan Mountains, Colorado: Part V. Epithermal mineralization from fluid mixing in the OH Vein. Eco. Geol. 92, 29–44.

Heald, P., Floey, N.K., Hayba, D.O., 1987. Comparative anatomy of volcanic-hosted epithermal deposits: Acid-sulfate and adularia-sericite types. Eco. Geol. 82, 1–26.

Hedenquist, J.W., Arribas, A., 1998. Evolution of an intrusion-centered hydrothermal system: Far southeast Lepanto porphyry and epithermal Cu–Au deposits, Philippines. Econ. Geol. 93, 373–404.

Hedenquist, J.W., Arribas, A.R., Gonzalez-Urien, E., 2000. Exploration for Epithermal Gold Deposits. Rev. Econ. Geol. 13, 245–277.

Hedenquist, J.W., Arribas, A., Reynolds, T.J., 1998. Evolution of an intrusion-centered hydrothermal system; Far Southeast-Lepanto porphyry and epithermal Cu–Au deposits, Philippines. Econ. Geol. 93 (4), 373–404.

Hedenquist, J.W., Henley, R.W., 1985. The importance of CO_2 on freezing point measurements of fluid inclusions: Evidence from active geothermal systems and implications for epithermal ore deposition. Econ. Geol. 80, 1379–1406.

Hedenquist, J.W., Lowenstern, J.B., 1994. The role of magmas in the formation of hydrothermal ore deposits. Nature 370, 519–527.

Henley, R.W., 1985. The geothermal framework for epithermal deposits. Rev. Econ. Geol. 2, 1–21.

Henley, B., Truesdell, A.H., Barton, P.B., Whitney, J.A., 1984. Fluid-mineral equilibria in hydrothermal systems. Rev. Econ. Geol. 1, 254–267.

Hirayama, K., Samimi, M., Zahedi, M., Hushmand-Zadeh, A., 1966. Geology of the Tarom district, western part (Zanjan area, north-west Iran). Geol. Surv. Iran, Rep. 8, 31 p.

Hosseinzadeh, M.R., Maghfouri, S., Moayyed, M., Rahmani, A., 2016. Khalifehlu deposit: High-sulfidation epithermal Cu-Au mineralization in the Tarom magmatic zone, north Khoramdareh. Sci. Quat. J. Geosci. 25 (99), 179–194 (in Persian with English abstract).

Irannezhadi, M.R., Ghorbani, M.R., Vossoughi, M., Pourmoafi, M., 2007. Tertiary arc-related volcanism in Central Alborz Mountains. Geoph. Res., Abs. 9, p. 867.

Izawa, E., Urashima, Y., Ibaraki, K., Suzuki, R., Yokoyama, T., Kawasaki, K., Koga, A., Taguchi, S., 1990. The Hishikari gold deposit: High-grade epithermal veins in Quaternary volcanics of southern Kyushu, Japan. J. Geochem. Expl. 36, 1–56.

John, D.A., 2001. Miocene and early Pliocene epithermal gold–silver deposits in the northern Great Basin, western USA: Characteristics, distribution, and relationship to magmatism. Eco. Geol. 96, 1827–1853.

John, D.A., Hofstra, A.H., Fleck, R.E., Brummer, J.E., Saderholm, E.C., 2003. Geological setting and genesis of the Mule Canyon low-sulfidation epithermal gold–silver deposit, north-central Nevada. Eco. Geol. 98, 425–463.

Johnson, C.A., Stricker, C.A., Gulbransen, C.A., Emmons, M.P., Determination of $\delta^{13}C$, $\delta^{15}N$, or $\delta^{34}S$ by isotope-ratio-monitoring mass spectrometry using an elemental analyzer: U.S. Geol. Surv. Tech. and Meth. in press.

Kan Iran Exploration Co., 1999, General exploration of Aliabad Mousavi copper deposit. Industry, Mine and Trade Organization of Zanjan (in Persian).

Klemm, L.M., Pettke, T., Heinrich, C.A., Campos, E., 2007. Hydrothermal evolution of the El Teniente deposit, Chile: Porphyry Cu–Mo ore deposition from low-salinity magmatic fluids. Econ. Geol. 102, 1021–1045.

Kouhestani, H., Azimzadeh, A.M., Mokhtari, M.A.A., Ebrahimi, M. 2017. Mineralization and fluid evolution of epithermal base metal veins from the Aqkand deposit, NW Iran. N. Jb. Miner. Abh. (J. Min. Geochem.) 194 (2), 139–155.

Kouhestani, H., Ghaderi, M., Chang, Z., Zaw, K., 2015. Constraints on the ore fluids in the Chah Zard breccia-hosted epithermal Au-Ag deposit, Iran: Fluid inclusions and stable isotope studies. Ore Geol. Rev. 65, 512–521.

Kouhestani, H., Mokhtari, M.A.A., 2013a. Final exploration report of copper in Aliabad-e Tazekand area. Industry, Mine and Trade Organization of Zanjan, 116 p. (in Persian).

Kouhestani, H., Mokhtari, M.A.A., 2013b. Geological and mineralization characteristics of Aliabad Cu occurrence, Tarom area, east of Zanjan. 17th Sym. of Geol. Soc. of Iran and the 1st Int. Cong. on Zagros Orogen, Tarbiat Modarres University, Tehran, Iran (in Persian).

Kouzmanov, K., Ramboz, C., 2003. Stable isotopic constrains on the origin of epithermal Cu-Au and related porphyry copper mineralizations in the southern Panagyurishte district, Srednogorie zone, Bulgaria. In: Eliopoulos, D.G., et al. (Eds.), Mineral exploration and sustainable development. Millpress, Rotterdam, p. 1181–1184.

Lattanzi, P., 1991. Applications of fluid inclusions in the study and exploration of mineral deposits. Eur. J. Mineral. 3, 689–697.

Li, Y.B., Liu, J.M., 2006. Calculation of sulfur isotope fractionation in sulfides. Geochim. Cosmochim. Acta 70, 1789–1795.

Liu, J., Mao, J.W., Wu, G., Wang, F., Luo, D.F., Hu, Y.Q., Li, T.G., 2014. Fluid inclusions and H–O–S–Pb isotope systematics of the Chalukou giant porphyry Mo deposit, Heilongjiang Province, China. Ore Geol. Rev. 59, 83–96.

Méheut, M., Lazzeri, M., Balan, E., Mauri, F., 2007. Equilibrium isotopic fractionation in the kaolinite, quartz, water system: Prediction from first-principles density-functional theory. Geochim. Cosmochim. Acta 71, 3170-3181.

Mehrabi, B., Ghasemi Siani, M., Goldfarb, R., Azizi, H., Ganerod, M., Marsh, E.E., 2016. Mineral assemblages, fluid evolution and genesis of polymetallic epithermal veins, Gulojeh district, NW Iran. Ore Geol. Rev. 78, 41–57.

Mehrabi, B., Tale Fazel, E., Ghasemi Siani, M., Eghbali, M.A., 2010. Investigation on mineralization and genetic model of Gulojeh Cu-Au vein deposit (north of Zanjan), using mineralogical, geochemical and fluid inclusion data. J. Sci. 35 (4), 185–199 (in Persian with English abstract).

Moayyed, M., 2001. Investigation of Tertiary volcano-plutonic bodies in west Alborz-Azarbayejan (Hashtjin area): Ph.D. thesis, University of Shahid Beheshti, Tehran, Iran. 296 p. (in Persian with English abstract).

Mokhtari, M.A.A., Kouhestani, H., Saeedi, A., 2016. Investigation on type and origin of copper mineralization at Aliabad Mousavi-Khanchy occurrence, east of Zanjan, using petrological, mineralogical and geochemical data. Sci. Qua. J. Geosci. 25 (100), 259–270 (in Persian with English abstract).

Moritz, R., Jackquat, S., Chambefort, I., Fontignie, D., 2003. Controls on ore formation at high sulfidation Au–Cu Chelopech deposit, Bulgaria: Evidence from infrared fluid inclusion microthermometry of enargite and isotope systematics of barite. In: Eliopoulos, D.G., et al. (Eds.), Mineral Exploration and Sustainable Development. Millpress, Rotterdam, pp. 1209–1212.

Nabatian, G., Ghaderi, M., 2013. Oxygen isotope and fluid inclusion study of the Sorkhe-Dizaj iron oxide-apatite deposit, NW Iran. Int. Geol. Rev. 55, 397–410.

Nabatian, G., Ghaderi, M., Corfu, F., Neubauer, F., Bernroider, M., Prokofiev, V., Honarmand, M., 2014b. Geology, alteration, age and origin of iron oxide–apatite deposits in Upper Eocene quartz monzonite, Zanjan district, NW Iran. Miner. Deposita 49 (2), 217–234.

Nabatian, G., Ghaderi, M., Daliran, F., Rashidnejad-Omran, N., 2013. Sorkhe-Dizaj iron oxide-apatite ore deposit in the Cenozoic Alborz–Azarbaijan magmatic belt, NW Iran. Res. Geol. 63, 42–56.

Nabatian, G., Ghaderi, M., Neubauer, F., Honarmandc, M., Xiaoming, L., Dong, Y, Jiang, S.H., Quadt, A., Bernroider, M., 2014a. Petrogenesis of Tarom high-potassic granitoids in the Alborz–Azarbaijan belt, Iran: Geochemical, U–Pb zircon and Sr–Nd–Pb isotopic constraints. Lithos 184-187, 324–345.

Nabatian, G., Jiang, S.Y., Honarmand, M., Neubauer, F., 2016. Zircon U–Pb ages, geochemical and Sr–Nd–Pb–Hf isotopic constraints on petrogenesis of the Tarom-Olya pluton, Alborz magmatic belt, NW Iran. Lithos 244, 43–58.

Naden, J., Killias, S.P., Darbyshire, D.P.F., 2005. Active geothermal system with entrained seawater as modern analogs for transitional volcanic-hosted massive sulfide and continental magmato-hydrothermal mineralization: The example of Milos Island, Greece. Geol. 33, 541–544.

Ohmoto, H., Rye, R.O., 1979. Isotopes of sulfur and carbon. In: Barnes, H.L. (Ed.), Geochemistry of Hydrothermal Ore Deposits. Wiley, New York, pp. 509–567.

Ouyang, H., Wu, X., Mao, J.W., Su, H., Santosh, M., Zhou, Z., Li, C., 2014. The nature and timing of ore formation in the Budunhua copper deposit, southern Great Xing'an Range: Evidence from geology, fluid inclusions, and U–Pb and Re–Os geochronology. Ore Geol. Rev. 63, 238–251.

Pirajno, F., 2009. Hydrothermal processes and mineral systems. Springer, Berlin, 1250 p.

Prokofiev, V.Y., Garofalo, P.S., Bortnikov, N.S., Kovalenker, V.A., Zorina, L.D., Grichuk, D.V., Selektor, S.L., 2010. Fluid inclusion constraints on the genesis of gold in the Darasun district (eastern Transbaikalia), Russia. Econ. Geol. 105, 395–416.

Rahmani, Sh., 2010. Gold exploration of Lohneh-Zardeh area (1:25000), Tarom zone. Geol. Surv. Iran, Rep. 121, 83 p. (in Persian).

Ramboz, C., Pichavant, M., Weisbrod, A., 1982. Fluid immiscibility in natural processes: Use and misuse of fluid inclusion data: II. Interpretation of fluid inclusion data in terms of immiscibility. Chem. Geol. 37, 29–48.

Richards, J.P., Bray, C.J., Channer, D.M. DeR, Spooner, E.T.C., 1997. Fluid chemistry and processes at the Porgera gold deposit, Papua New Guinea. Miner. Deposita 32, 119–132.

Roedder, E., 1984. Fluid inclusions. Rev. Mineral. 12, 644 p.

Roedder, E., Bodnar, R.J., 1980. Geologic pressure determinations from fluid inclusion studies. Annu. Rev. Earth Planet. Sci. 8, 263–301.

Ronacher, E., Richards, J.P., Johnston, M.D., 2000. Evidence for fluid phase separation in high-grade ore zones at the Porgera gold deposit, Papua New Guinea. Miner. Deposita 35, 683–688.

Rosso, K.M., Bodnar, R.J., 1995. Microthermometric and Raman spectroscopic detection limits of CO_2 in fluid inclusions and the Raman spectroscopic characterization of CO_2. Geochim. Cosmochim. Acta 59 (19), 3961–3975.

Rusk, B.G., Reed, M.H., Dilles, J.H., 2008. Fluid inclusion evidence for magmatic-hydrothermal fluid evolution in the porphyry copper-molybdenum deposit at Butte, Montana. Econ. Geol. 103 (2), 307–334.

Rye, R., 1993. Evolution of magmatic fluids in the epithermal environment: The stable isotope perspective. Econ. Geol. 88, 733–753.

Sabeva, R., Mladenova, V., Mogessie, A., 2017. Ore petrology, hydrothermal alteration, fluid inclusions, and sulfur stable isotopes of the Milin Kamak intermediate sulfidation epithermal Au-Ag deposit in Western Srednogorie, Bulgaria. Ore Geol. Rev. 88, 400–415.

Saeedi, A., Mokhtari, M.A.A., Kouhestani, H., 2017. Petrology and geochemistry of granitoids at Khanchy-Aliabad region, Tarom sub-zone, East of Zanjan. J. Petrology, in press (in Persian with English abstract).

Scott, A.M., Watanabe, Y., 1998. Extreme boiling model for variable salinity of the Hokko low-sulfidation epithermal Au prospect, southwestern Hokkaido, Japan. Miner. Deposita 33, 568–578.

Sharp, Z.D., 1990. A laser-based microanalytical method for the in situ determination of oxygen isotope ratios of silicates and oxides. Geochim. Cosmochim. Acta 54, 1353–1357.

Sherlock, R.L., Tosdal, R.M., Lehrman, N.J., Graney, J.R., Losh, S., Jowett, E.C., Kesler, S.E., 1995. Origin of the McLaughlin mine sheeted vein complex: Metal zoning, fluid inclusion and isotopic evidence. Econ. Geol. 90, 2156–2181.

Siahcheshm, K., Calagari, A.A., Abedini, A., 2014. Hydrothermal evolution in the Maher–Abad porphyry Cu–Au deposit, SW Birjand, Eastern Iran: Evidence from fluid inclusions. Ore Geol. Rev. 58, 1–13.

Sillitoe, R.H., Hedenquist, J.W., 2003. Linkages between volcanotectonic settings, ore fluid compositions, and epithermal precious-metal deposits. Econ. Geol. Spec. Pub. 10, 315–343.

Simeone, R., Simmons, S.F., 1999. Mineralogical and fluid inclusion studies of low-sulfidation epithermal veins at Osilo (Sardinia), Italy. Miner. Deposita 34, 705–717.

Simmons, S.F., 1995. Magmatic contributions to low-sulfidation epithermal deposits. In: Thompson, J.F. (Ed.), Magmas, Fluids and Ore Deposits. Mineral. Assoc. of Can. 455–477.

Simmons, S.F., Arehart, G., Simpson, M.P., Mauk, J.L., 2000. Origin of massive calcite veins in the Golden Cross low-sulfidation, epithermal Au–Ag deposit, New Zealand. Eco. Geol. 95, 99–112.

Simmons, S.F., Browne, P.R.L., 2000. Hydrothermal minerals and precious metals in the Broadlands-Ohaaki geothermal system: Implications for understanding low-sulfidation epithermal environments. Eco. Geol. 95, 971–1000.

Simmons, S.F., White, N.C., John, D.A., 2005. Geological characteristics of epithermal precious and base metal deposits. In: Hedenquist, J.W., Thompson, J.F.H., Goldfarb, J.R., Richards, J.P. (Eds.), Econ. Geol. 100th Ann. Vol., pp. 485–522.

Simon, G., Kesler, S.E., Russell, N., Hall, C.M., Bell, D., Pinero, E., 1999. Epithermal gold mineralization in an old volcanic arc: The Jacinto deposit, Camaguey district, Cuba. Econ. Geol. 94, 487–506.

Simpson, M.P., Mauk, J.L., Simmons, S.F., 2001. Hydrothermal alteration and hydrologic evolution of the Golden Cross epithermal Au–Ag deposit, New Zealand. Econ. Geol. 96, 773–796.

Spycher, N.F., Reed, M.H., 1989. Evolution of a Broadlands-type epithermal ore fluid along alternative P–T paths: Implications for the transport and deposition of base, precious, and volatile metals. Econ. Geol. 84, 328–359.

Steele-MacInnis, M., Bodnar, R.J., Naden, J., 2011. Numerical model to determine the composition of H_2O–NaCl–$CaCl_2$ fluid inclusions based on microthermometric and microanalytical data. Geochim. Cosmochim. Acta 75, 21– 40.

Stöcklin, J., Eftekheārnezhād, J., 1969. Geological map of Zanjan, scale: 1:250,000. Geol. Surv. Iran.

Taylor, H.P., 1968. The oxygen isotope geochemistry of igneous rocks. Contrib. Mineral. Petrol. 19, 1–71.

Thiersch, P.C., Williams-Jones, A.E., Clark, J.R., 1997. Epithermal mineralization and ore controls of the Shasta Au–Ag deposit, Toodoggone District, British Columbia, Canada. Miner. Deposita 32, 44–57.

Urusova, M.A., 1975. Volume properties of aqueous solutions of sodiumchloride at elevated temperatures and pressures. Russ. J. Inorg. Chem. 20, 1717–1721.

Vallance, J., Boiron, M., Cathelineau, M., Fourcade, S., Varlet, M., Marignac, C., 2004. The granite hosted gold deposit of Moulin de Cheni (Saint-Yrieix district, Massif Central, France): Petrographic, structural, fluid inclusion and oxygen isotope constraints. Miner. Deposita 39, 265–281.

Vallance, J., Cathelineau, M., Boiron, M.C., Fourcade, S., Shepherd, T.J., Naden, J., 2003. Fluid–rock interactions and the role of late Hercynian aplite intrusion in the genesis of the Castromil gold deposit, northern Portugal: Chem. Geol. 194, 201–224.

Van Den Kerkhof, A.M., Hein, U.F., 2001. Fluid inclusion petrography. In: Andersen, T., Frezzotti, M.L., Burke, E.A.J., (Eds.), Fluid inclusions: phase relationships–methods applications (special issue). Lithos 55 (1–4), 320 p.

Verdel, C., Wernicke, B.P., Hassanzadeh, J., Guest, B., 2011. A Paleogene extensional arc flare-up in Iran. Tectonics 30 (3). http://dx.doi.org/10.1029/2010TC002809 (TC3008).

Wang, Y., Sasaki, M., Sasada, M., Chen, C.H., 1999. Fluid inclusion studies of the Chinkuashih high-sulfidation gold–copper deposits in Taiwan. Chem. Geol. 154, 155–167.

White, N.C., Hedenquist, J.W., 1990. Epithermal environments and styles of mineralization: Variations and their causes, and guidelines for exploration. J. Geochem. Expl. 36, 445–474.

White, N.C., Hedenquist, J.W., 1995. Epithermal gold deposits: Styles, characteristics and exploration. SEG News l, 27, 1–13.

Whitney, D.L., Evans, B.W., 2010. Abbreviations for names of rock-forming minerals. Am. Mineral. 95, 185–187.

Wilkinson, J.J., 2001. Fluid inclusions in hydrothermal ore deposits. Lithos 55, 229–272.

Yasami, N., Ghaderi, M., Madanipour, S., Taghilou, B., 2017. Structural control on overprinting high-sulfidation epithermal on porphyry mineralization in the Chodarchay deposit, northwestern Iran. Ore Geol. Rev. 86, 212–224.

Yilmaz, H., Oyman, O., Arehart, G.B., Colakoglu, A.R., Billor, Z., 2007. Low-sulfidation type Au–Ag mineralization at Bergama, Izmir, Turkey. Ore Geol. Rev. 32, 81–124.

Yilmaz, H., Oyman, T., Sonmez, F.N., Arehart, G.B., Billor, Z., 2010. Intermediate sulfidation epithermal gold-base metal deposits in Tertiary subaerial volcanic rocks, Sahinli/Tespih Dere (Lapseki/Western Turkey). Ore Geol. Rev. 37, 236–258.

Zamanian, H., Rahmani, Sh., Jannesari, M.R., Zareii Sahamieh, R., Borna, B., 2016. Ore genesis study of the Cu-Au vein type deposit in the Tarom granitoid (north Zanjan) based on mineralogical, geochemical and fluid inclusion evidences. Sci. Qua. J. Geosci., 98, 255–282 (in Persian with English abstract).

Zhai, D.G., Liu, J.J., Wang, J.P., Yao, M.J., Wu, S.H., Fu, C., Liu, Z.J., Wang, S.G., Li, Y.X., 2013. Fluid evolution of the Jiawula Ag–Pb–Zn deposit, Inner Mongolia: Mineralogical, fluid inclusion, and stable isotopic evidence. Int. Geol. Rev. 55 (2), 204–224.

Zhai, W., Sun, X., Sun, W., Su, L., He, X., Wu, Y., 2009. Geology, geochemistry, and genesis of Axi: A Paleozoic low-sulfidation type epithermal gold deposit in Xinjiang, China. Ore Geol. Rev. 36 (4), 265–281.

Zhang, J., Chen, Y.J., Pirajno, F., Deng, J., Chen, H.Y., Wang, C.M., 2013. Geology, C–H–O–S–Pb isotope systematics and geochronology of the Yindongpo gold deposit, Tongbai Mountains, central China: Implication for ore genesis. Ore Geol. Rev. 53, 343–356.

Zhang, Y., Frantz, J.D., 1987. Determination of the homogenization temperatures and densities of supercritical fluids in the system NaCl–KCI–$CaCl_2$–H_2O using synthetic fluid inclusions. Chem. Geol. 64, 335–350.

FIGURE CAPTIONS:

Fig. 1. A. Sketch map showing the position of the Alborz magmatic arc (modified after Alavi, 1991; Aghanabati, 2004), together with the location of the THMB. B. Regional geology of the THMB (modified from Ghorbani, 2013) showing location of the Aliabad-Khanchy and other epithermal precious and base metal deposits. 1- Gulojeh, 2- Rashtabad, 3- Aqkand, 4- Jalilabad, 5- Aliabad-Khanchy, 6- Lohneh, 7- Chodarchay, 8- Khalyfehlou.

Fig. 2. Simplified geological map of the Aliabad-Khanchy area (modified after Kouhestani and Mokhtari, 2013a); inset shows schematic cross-section through the deposit.

Fig. 3. Stratigraphic column of the host rock lithologies at Aliabad-Khanchy area.

Fig. 4. Field photographs showing the Cu-bearing brecciated quartz veins at the Aliabad-Khanchy epithermal base metal deposit. A, B. The Cu-bearing quartz veins at Aliabad that crosscut the volcaniclastic (crystal tuff, lithic crystal tuff) host rocks. C. Parallel sheeted mineralized quartz veins at Aliabad cutting volcaniclastic host rocks. D. The NE-trending mineralized vein at Khanchy that crosscut the crystal tuff host rocks. E. Stockwork Cu-bearing quartz veinlets within the altered host andesitic lava at Khanchy.

Fig. 5. Photomicrographs (transmitted polarized-light, XPL) illustrating mineralization stages at Aliabad-Khanchy epithermal base metal deposit. A. Rounded clast of stage 1 chalcopyrite in host crystal tuff. B. Subrounded clast of stage 1 mineralization in quartz-sulfide cement of stage 2. The clast contains quartz-chalcopyrite veinlets; chalcopyrite altered to malachite. C. Stage 2 quartz-sulfide veinlet. D. Stage 2 breccia with quartz and chalcopyrite cement. E. Subparallel sheeted stage 3 quartz veins crosscutting stage 2 quartz-sulfide veinlet and in turn, cut by stage 4 veinlets. F. Stage 4 mineralization as hematite-bearing quartz veins crosscutting stage 2 veins. G. Stage 5 chlorite veinlets cutting stage 2 quartz-chalcopyrite veins. H. Stage 5 chlorite filling the vugs of stage 2 quartz-chalcopyrite cement. *A-L: andesitic lava lithic, C-Qz: crystalline quartz, Ccp: chalcopyrite, Chl: chlorite, Cv: covellite, Ep: epidote,*

Gth: goethite, Hem: hematite, M-Qz: microcrystalline quartz, Mlc: malachite, Pl: plagioclase, Py: pyrite, Qz: quartz, Ser: sericite. Mineral abbreviations follow Whitney and Evans (2010).

Fig. 6. Photomicrographs (transmitted polarized-light, XPL) of wall-rock alteration types at Aliabad-Khanchy epithermal base metal deposit. A, B. Silica alteration occurs as breccia cement (A) and stockwork quartz veins (B). C. Brown chlorite with spheroidal texture in chlorite alteration. D. Alteration of plagioclase to sericite in argillic zone. E, F. Alteration of plagioclase and pyroxene to sericite, calcite and epidote in propylitic zone. Chloritized groundmass can be observed in F. Abbreviations as in Fig. 5.
Fig. 7. Reflected light (A-D) and plane polarized transmitted light (E-F) photomicrographs of ore and gangue mineralogy and textures at the Aliabad-Khanchy epithermal base metal deposit. A and B. Anhedral crystals of chalcopyrite replaced by supergene goethite (A) and covellite (B). C. Anhedral crystals of pyrite replaced by goethite. D. Bladed crystals of hematite. E. Malachite with vug infill texture. Two episodes of quartz deposition are also observed. F-H. Microcrystalline and crystalline quartz with comb (F), colloform/crustiform (G) and cockade (H) textures. Abbreviations as in Fig. 5.

Fig. 8. Paragenetic sequence showing the relative abundance, structure and texture of gangue and ore minerals at the Aliabad-Khanchy epithermal base metal deposit.

Fig. 9. Photomicrographs (at room temperature in plane-polarized light, PPL) of the fluid inclusions in quartz from the Aliabad-Khanchy deposit. A and B. Coexisting primary LV, L and V fluid inclusions. C. Isolated primary VL fluid inclusion. D. Coexisting primary VL and LV fluid inclusions, implying for fluid boiling. L = liquid, V = vapor, PS = pseudosecondary fluid inclusions.

Fig. 10. Frequency histograms of final ice-melting temperatures (A), weight ratio of $NaCl/(NaCl+CaCl_2)$ (B), homogenization temperatures (C), and salinities (D) for the primary LV inclusions in internally consistent fluid inclusion assemblages from the Aliabad-Khanchy deposit. The relative proportions of Na and Ca are derived from the $H_2O–NaCl–CaCl_2$ system (Steele-MacInnis et al., 2011), see Fig. 12.

Fig. 11. T_h-salinity diagram for LV fluid inclusion assemblages from the Aliabad-Khanchy deposit. The dashed lines show densities (g/cm^3) of fluid inclusions (after Wilkinson, 2001).

Fig. 12. Ternary plot of phase relations in the $H_2O–NaCl–CaCl_2$ system, with the composition of the fluid inclusions from Aliabad-Khanchy deposit calculated by the methodology of Steele-MacInnis et al. (2011). The solid lines represent cotectic curves that separate the stability fields of ice (I), halite (H), hydrohalite (HH), and antarciticite (A). Shown are $NaCl/(NaCl+CaCl_2)$ weight fractions for fluid inclusions obtained from final hydrohalite melting temperatures.

Fig. 13. T_h-salinity diagram for fluid inclusion data at the Aliabad-Khanchy deposit showing mixing and/or boiling trend during evolution of hydrothermal fluids. The hypothetical compositions of magmatic and meteoric waters are plotted according to Lattanzi (1991), Hedenquist and Arribas (1998) and Naden et al. (2005).

Fig. 14. Pressure estimates for fluid inclusions in the Aliabad-Khanchy deposit that exhibited final homogenization by vapor disappearance of LV fluid inclusions (modified after Bouzari and Clark, 2006).

Fig. 15. Schematic genetic model for the Aliabad-Khanchy deposit (see Figs. 2 and 3 for lithology). The model shows magmatic fluids derived from magma that mix with deeply circulating meteoric water, forming the Cu-bearing quartz veins.

TABLE CAPTIONS:

Table 1. Summary table describing the main characteristics of each mineralization stages at Aliabad-Khanchy epithermal base metal deposit.

Table 2**.** Microthermometric data summary of LV fluid inclusion assemblages from Aliabad-Khanchy epithermal base metal deposit.

Table 3. Stable isotope data (‰) for the Aliabad-Khanchy epithermal base metal deposit.

Highlights:

- New data on ore mineralogy and genesis of the Aliabad-Khanchy deposit, Tarom-Hashtjin metallogenic belt (THMB), northwest Iran.
- Hydrothermal fluid was characterized by fluid mixing and dilution.
- Stable isotopes suggest the ore–fluid system evolved from magmatic to meteoric.
- The Aliabad-Khanchy deposit could be classified as intermediate-sulfidation style of epithermal mineralization.
- Genetic links between epithermal mineralization and late Eocene magmatism at THMB.

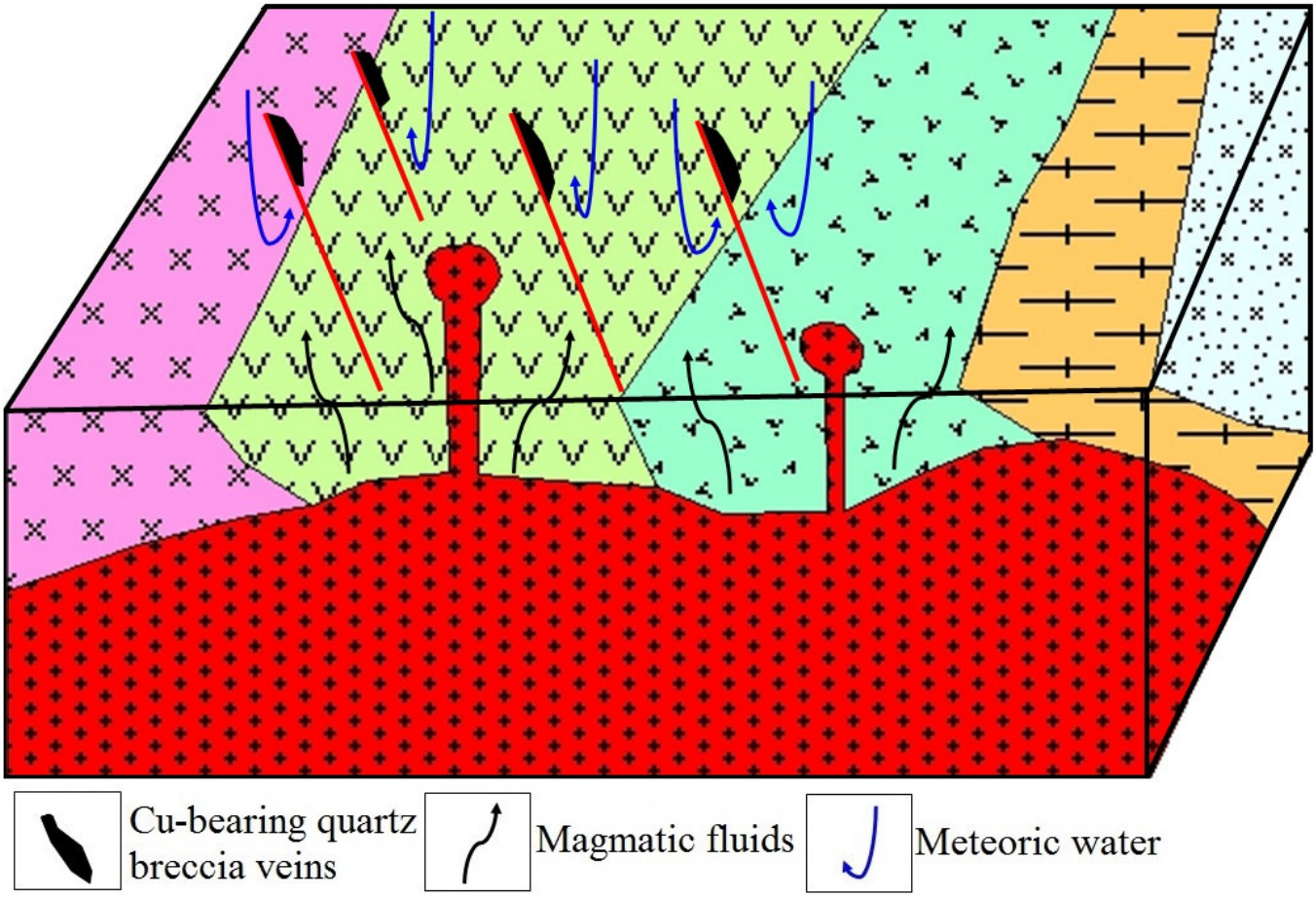

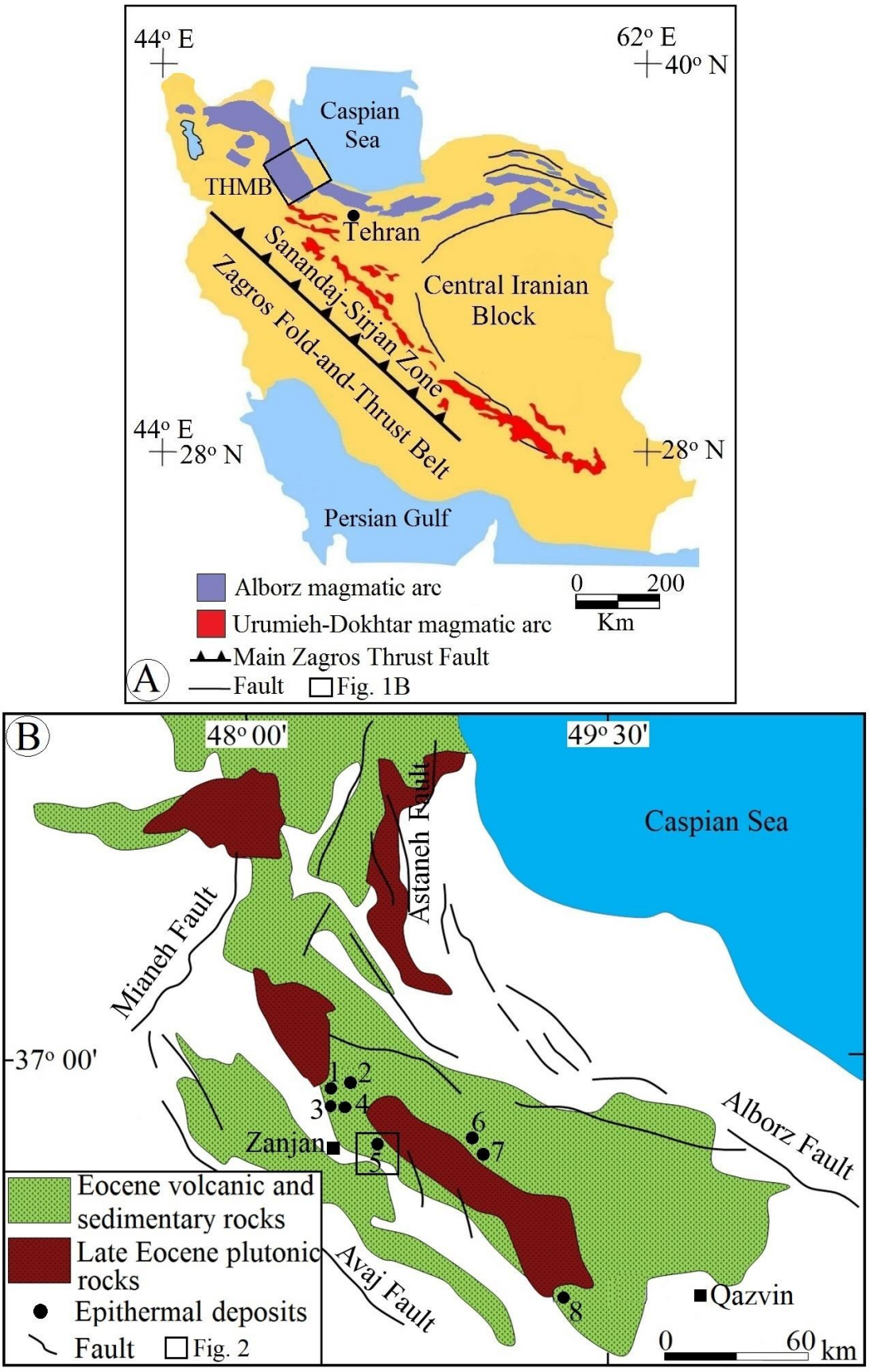

Fig. 1

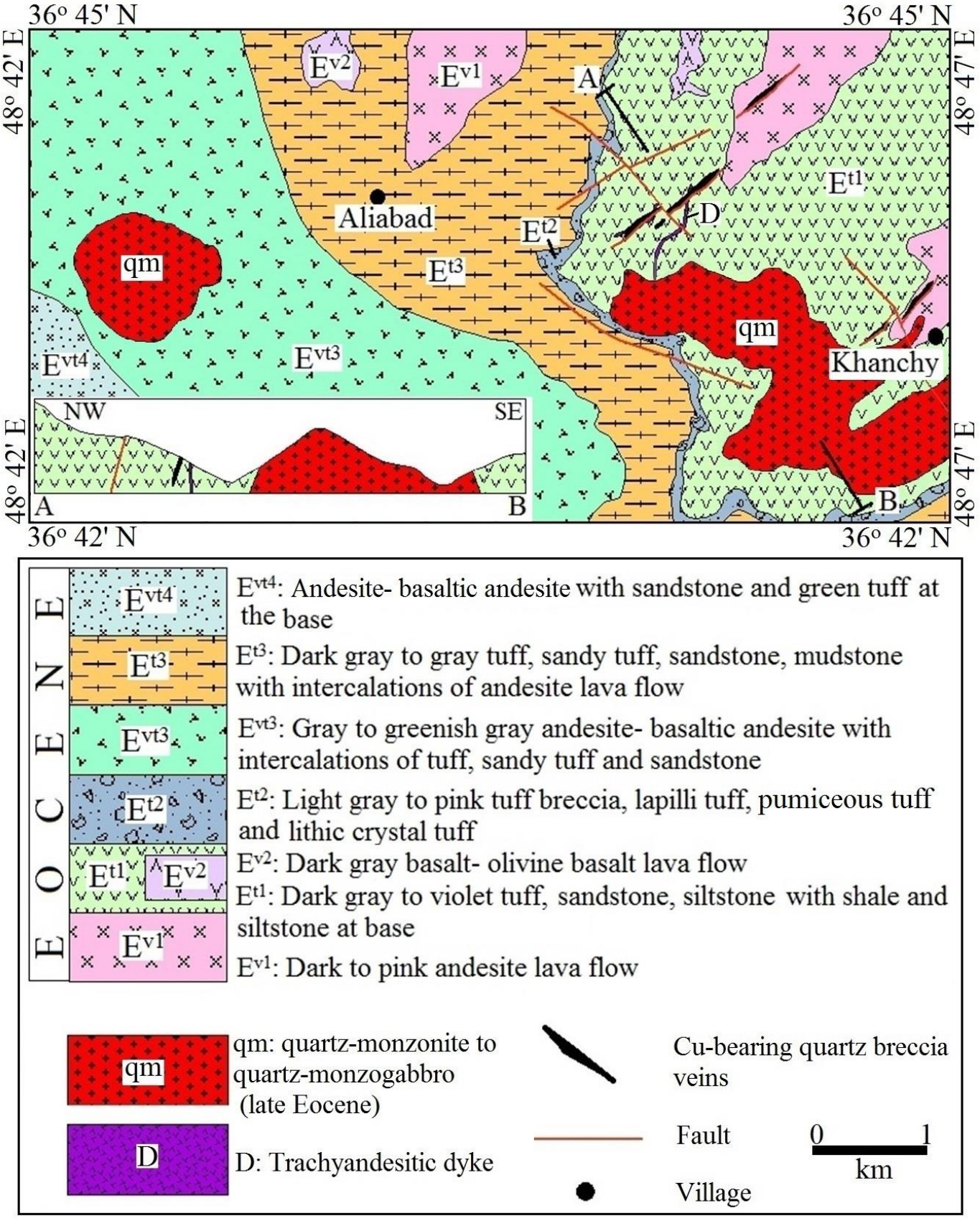
36° 45' N
36° 45' N
48° 42' E
48° 47' E
Ev2
Ev1
A
Et1
Aliabad
D
Et2
Et3
qm
qm
Evt4
Evt3
Khanchy
NW
SE
A
B
B
48° 42' E
48° 47' E
36° 42' N
36° 42' N
EOCENE
Evt4: Andesite- basaltic andesite with sandstone and green tuff at the base
Et3: Dark gray to gray tuff, sandy tuff, sandstone, mudstone with intercalations of andesite lava flow
Evt3: Gray to greenish gray andesite- basaltic andesite with intercalations of tuff, sandy tuff and sandstone
Et2: Light gray to pink tuff breccia, lapilli tuff, pumiceous tuff and lithic crystal tuff
Ev2: Dark gray basalt- olivine basalt lava flow
Et1: Dark gray to violet tuff, sandstone, siltstone with shale and siltstone at base
Ev1: Dark to pink andesite lava flow
qm
qm: quartz-monzonite to quartz-monzogabbro (late Eocene)
D
D: Trachyandesitic dyke
Cu-bearing quartz breccia veins
Fault
Village
0
1
km

Fig. 2

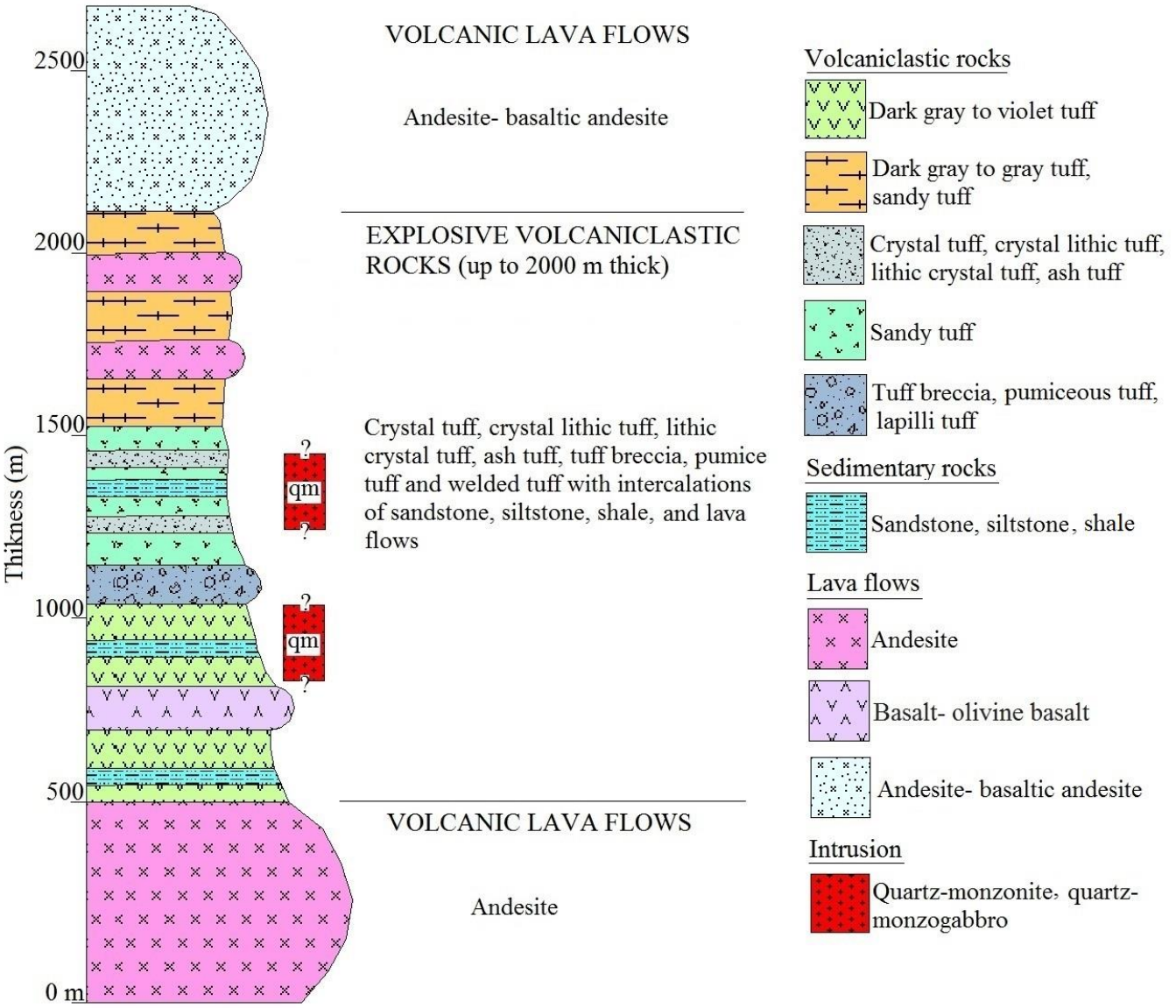

Fig. 3

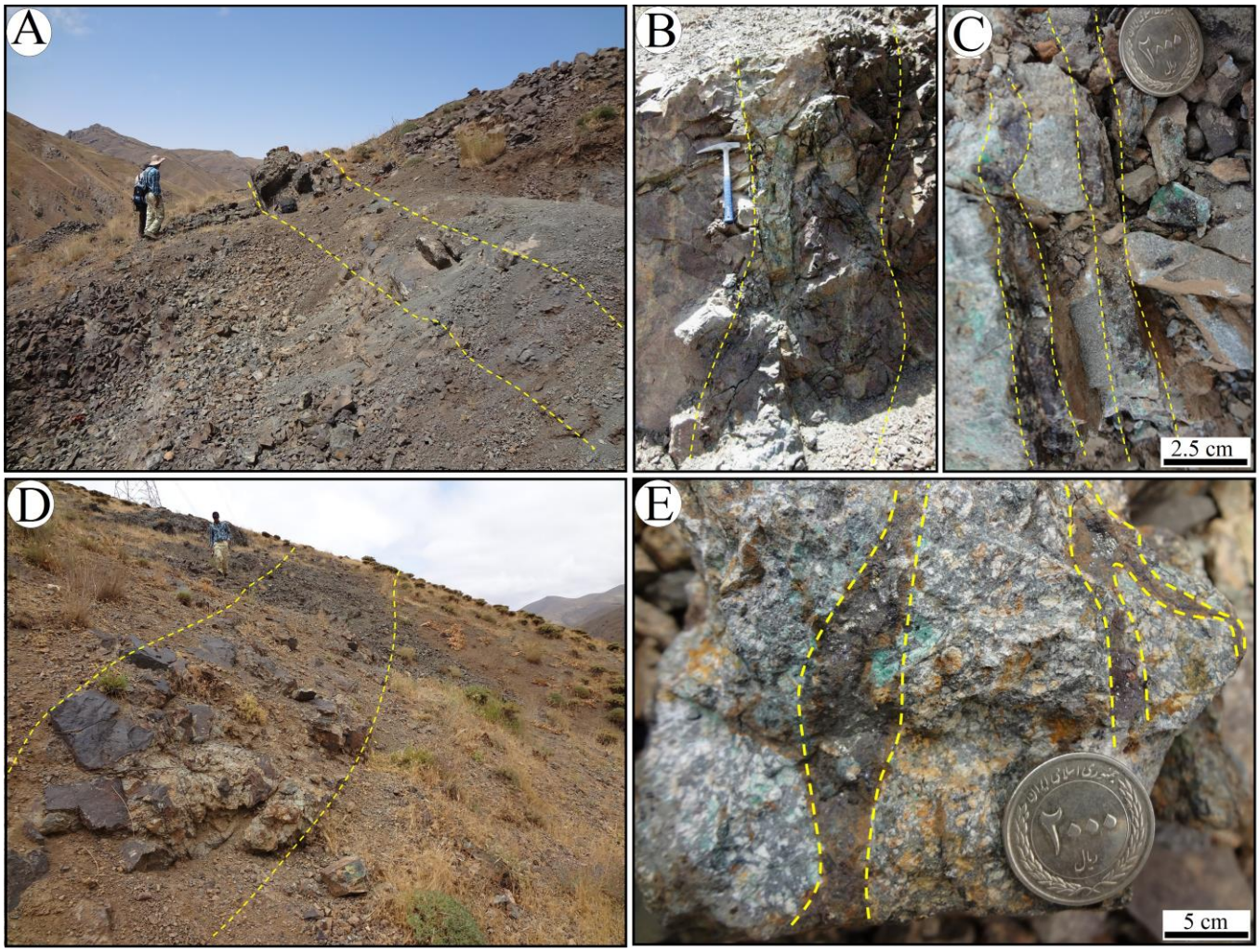

Fig. 4

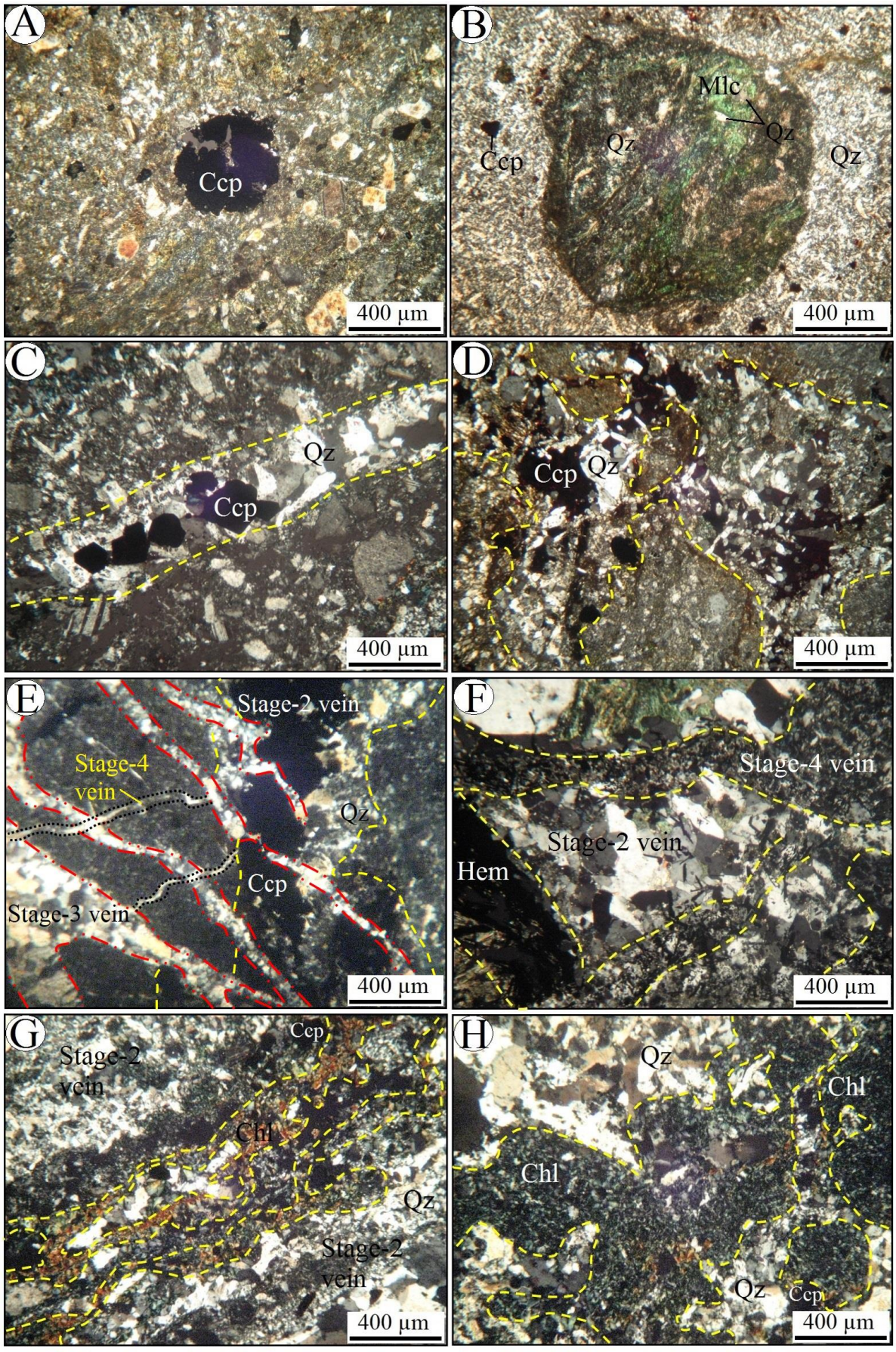
A
Ccp
400 μm
B
Mlc
Qz
Qz
Ccp
Qz
400 μm
C
Qz
Ccp
400 μm
D
Ccp
Qz
400 μm
E
Stage-2 vein
Stage-4
vein
Qz
Ccp
Stage-3 vein
400 μm
F
Stage-4 vein
Stage-2 vein
Hem
400 μm
G
Ccp
Stage-2
vein
Chl
Qz
Stage-2
vein
400 μm
H
Qz
Chl
Chl
Qz
Ccp
400 μm

Fig. 5

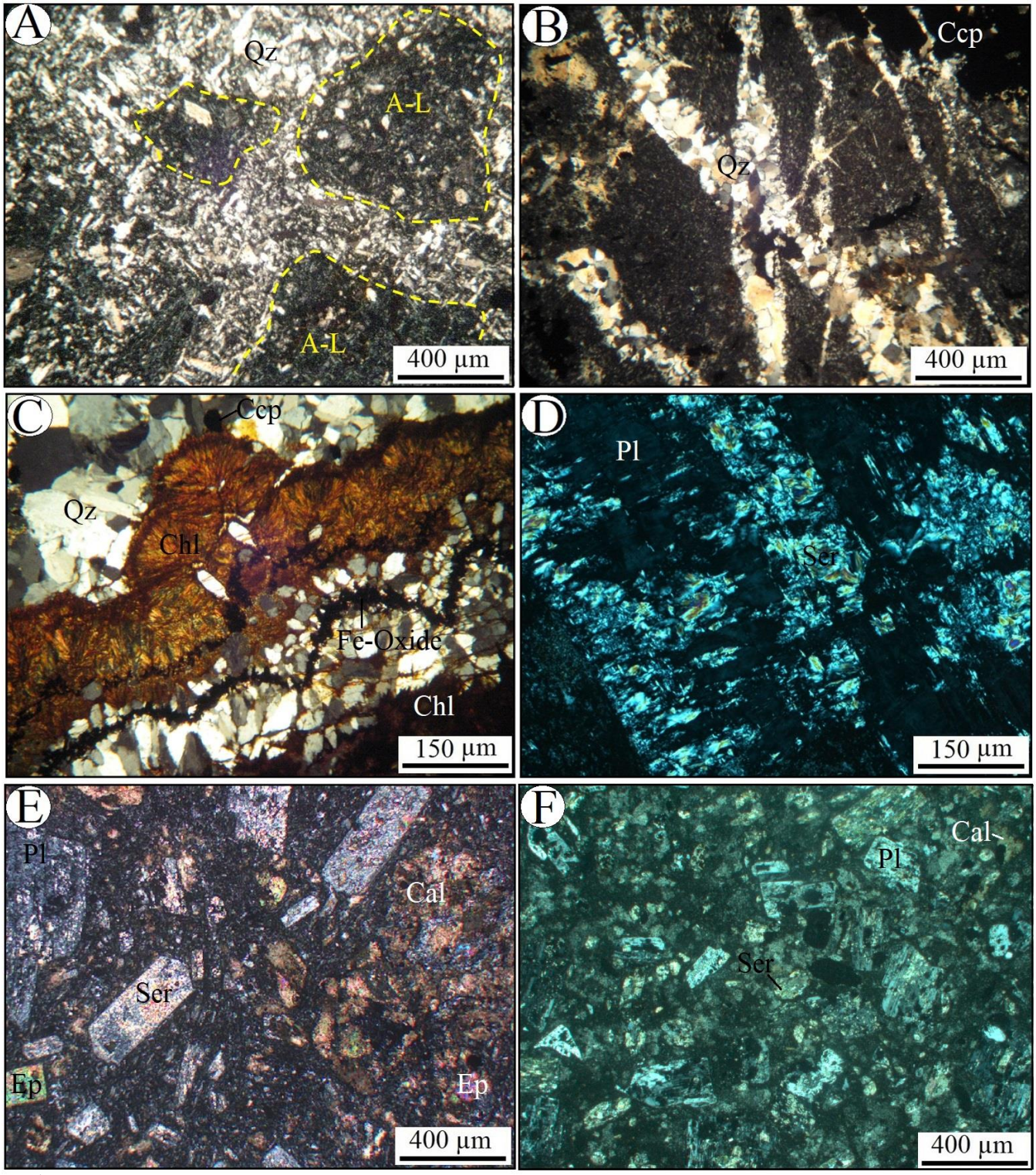
A
Qz
A-L
A-L
400 µm
B
Ccp
Qz
400 µm
C
Ccp
Qz
Chl
Fe-Oxide
Chl
150 µm
D
Pl
Ser
150 µm
E
Pl
Cal
Ser
Ep
Ep
400 µm
F
Cal
Pl
Ser
400 µm

Fig. 6

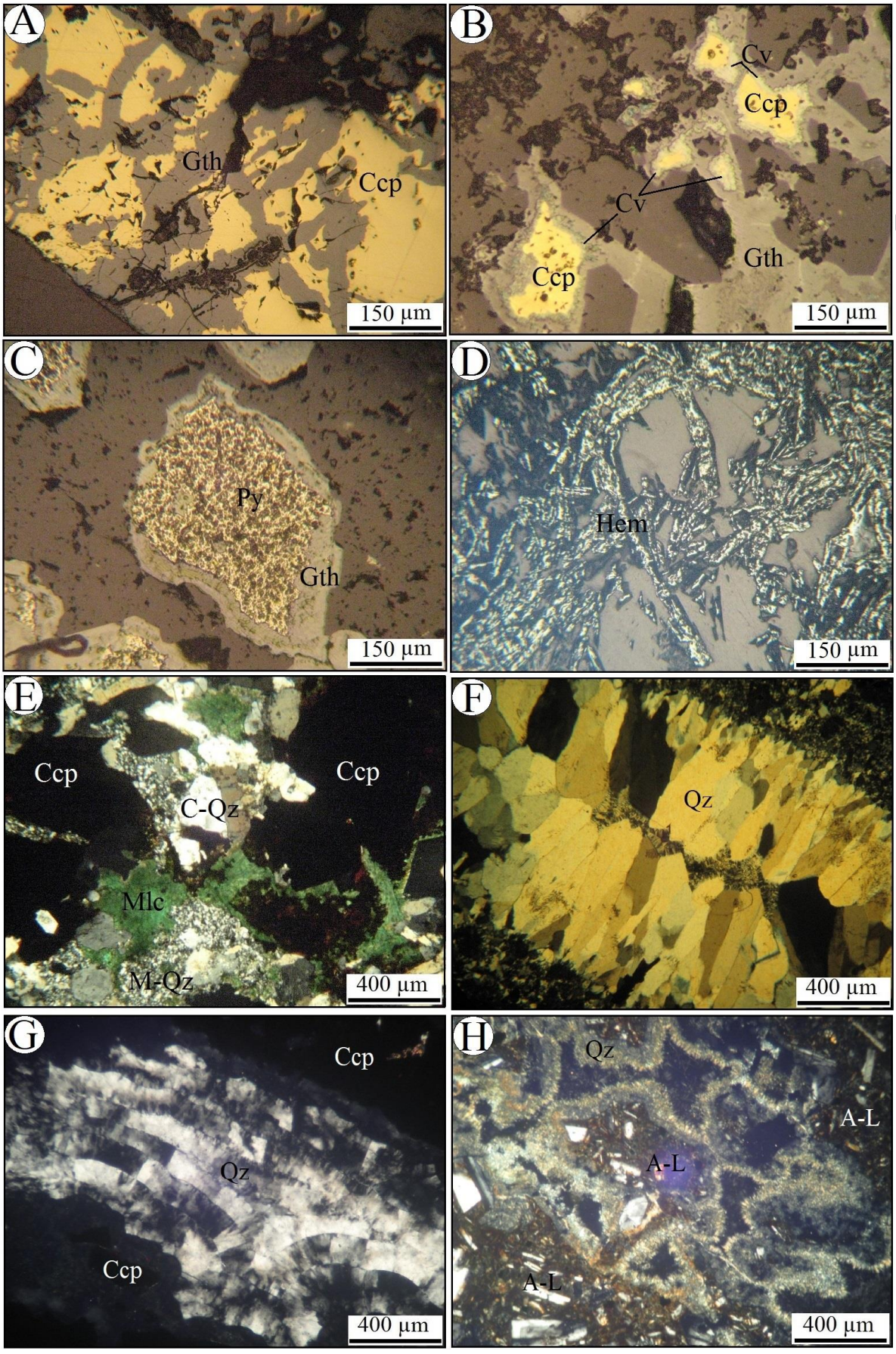
A
Gth
Ccp
150 µm
B
Cv
Ccp
Cv
Ccp
Gth
150 µm
C
Py
Gth
150 µm
D
Hem
150 µm
E
Ccp
Ccp
C-Qz
Mlc
M-Qz
400 µm
F
Qz
400 µm
G
Ccp
Qz
Ccp
400 µm
H
Qz
A-L
A-L
A-L
400 µm

Fig. 7

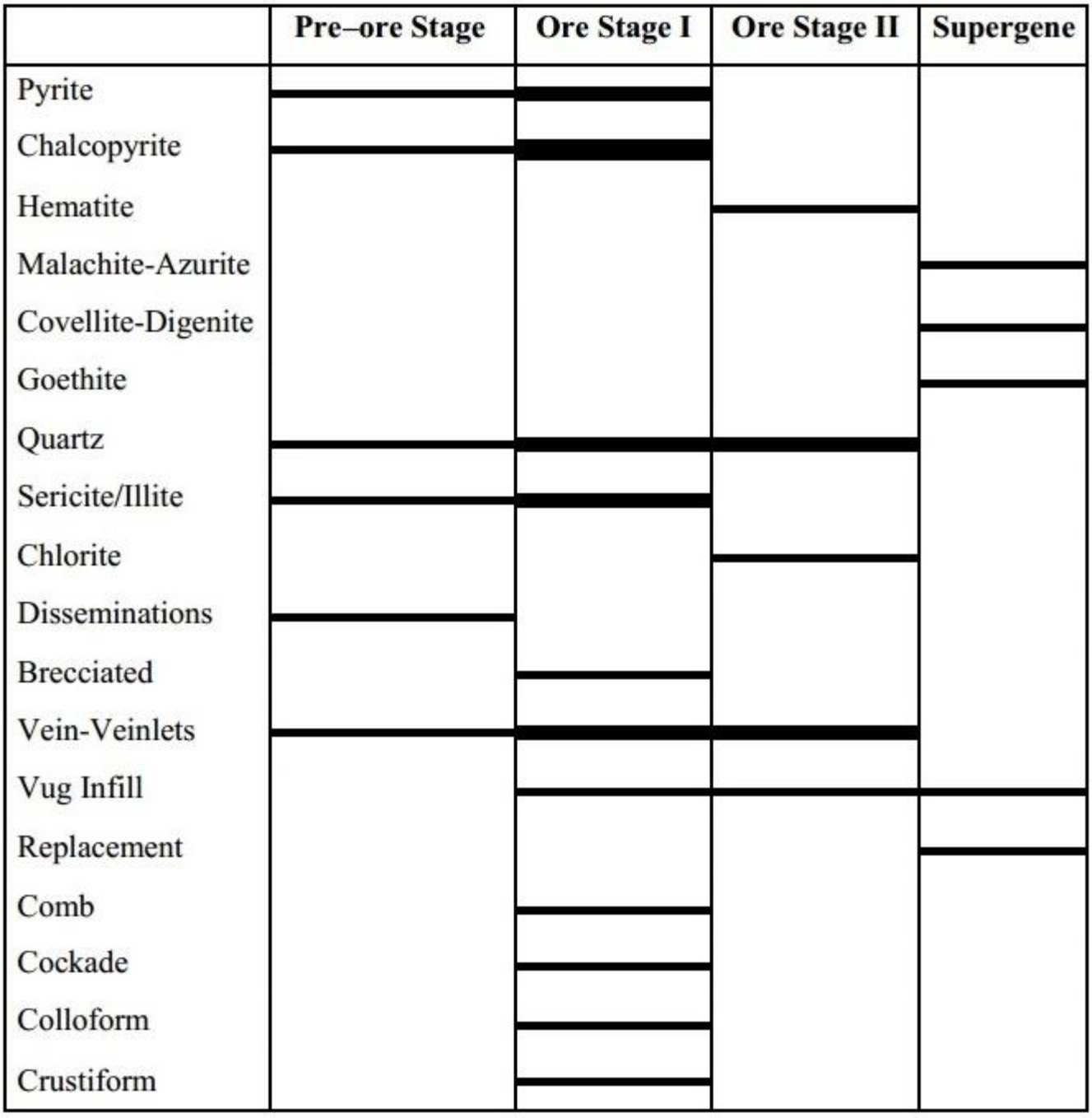

Fig. 8

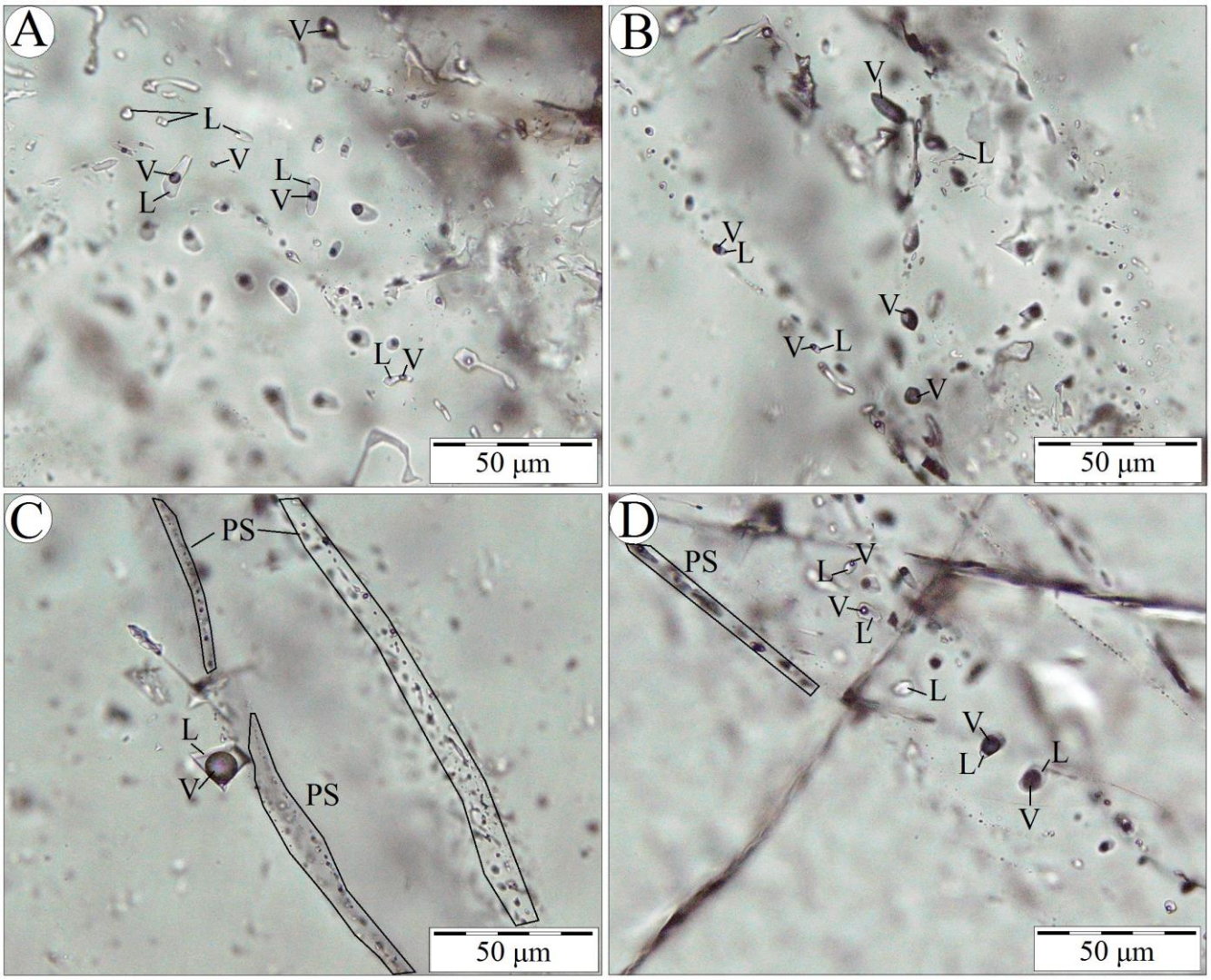

Fig. 9

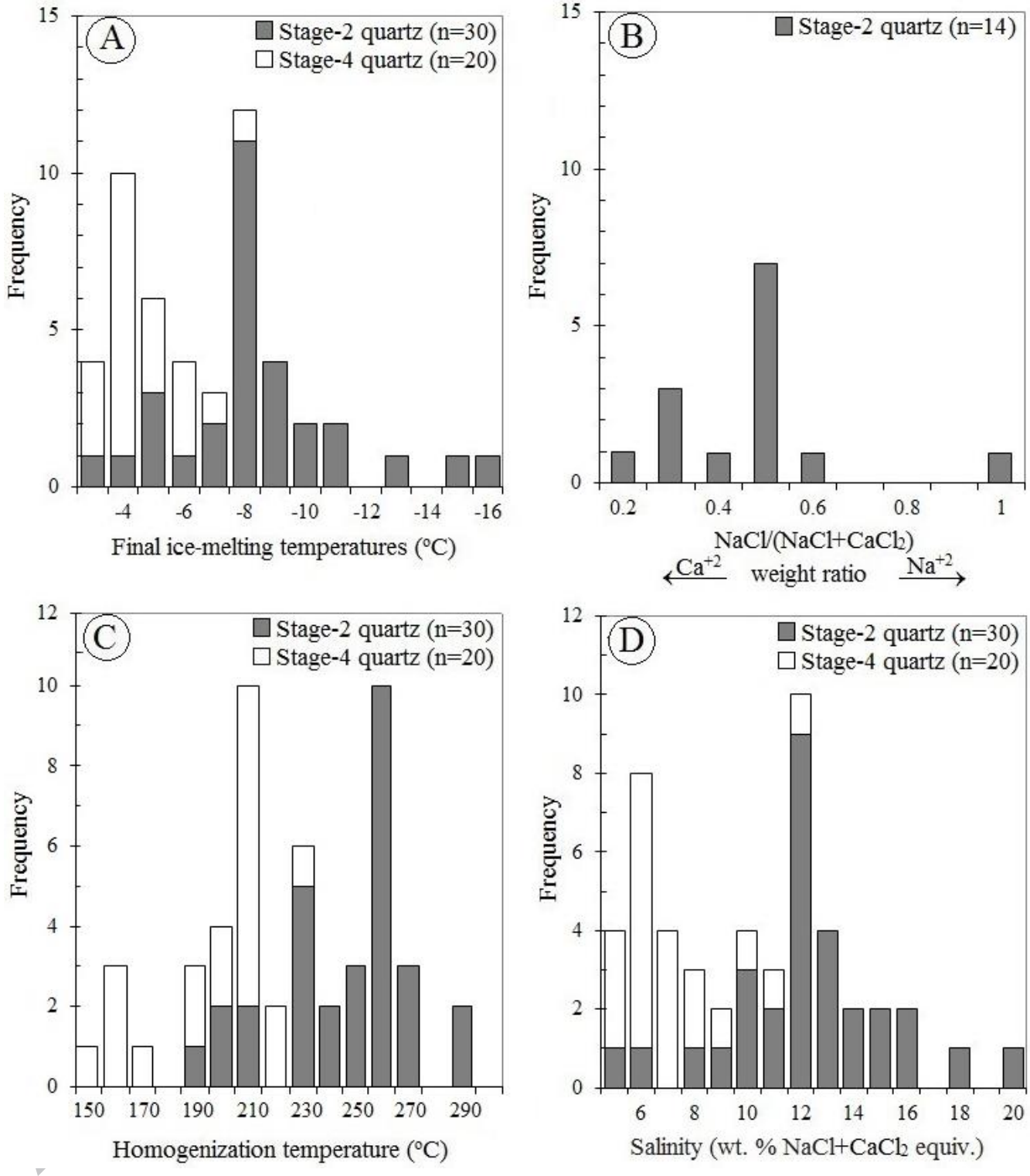
A
Stage-2 quartz (n=30)
Stage-4 quartz (n=20)
Frequency
Final ice-melting temperatures (°C)
B
Stage-2 quartz (n=14)
Frequency
NaCl/(NaCl+CaCl2)
Ca+2 weight ratio Na+2
C
Stage-2 quartz (n=30)
Stage-4 quartz (n=20)
Frequency
Homogenization temperature (°C)
D
Stage-2 quartz (n=30)
Stage-4 quartz (n=20)
Frequency
Salinity (wt. % NaCl+CaCl2 equiv.)

Fig. 10

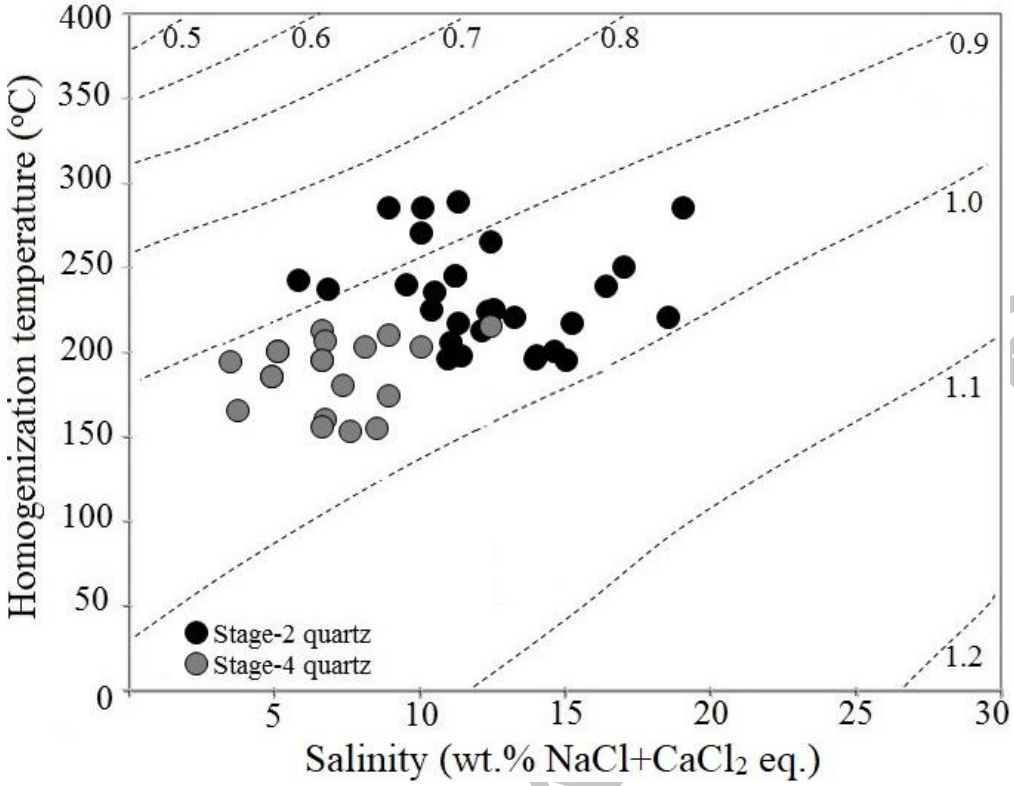
Homogenization temperature (°C)
Salinity (wt.% NaCl+CaCl2 eq.)
0.5
0.6
0.7
0.8
0.9
1.0
1.1
1.2
Stage-2 quartz
Stage-4 quartz

Fig. 11

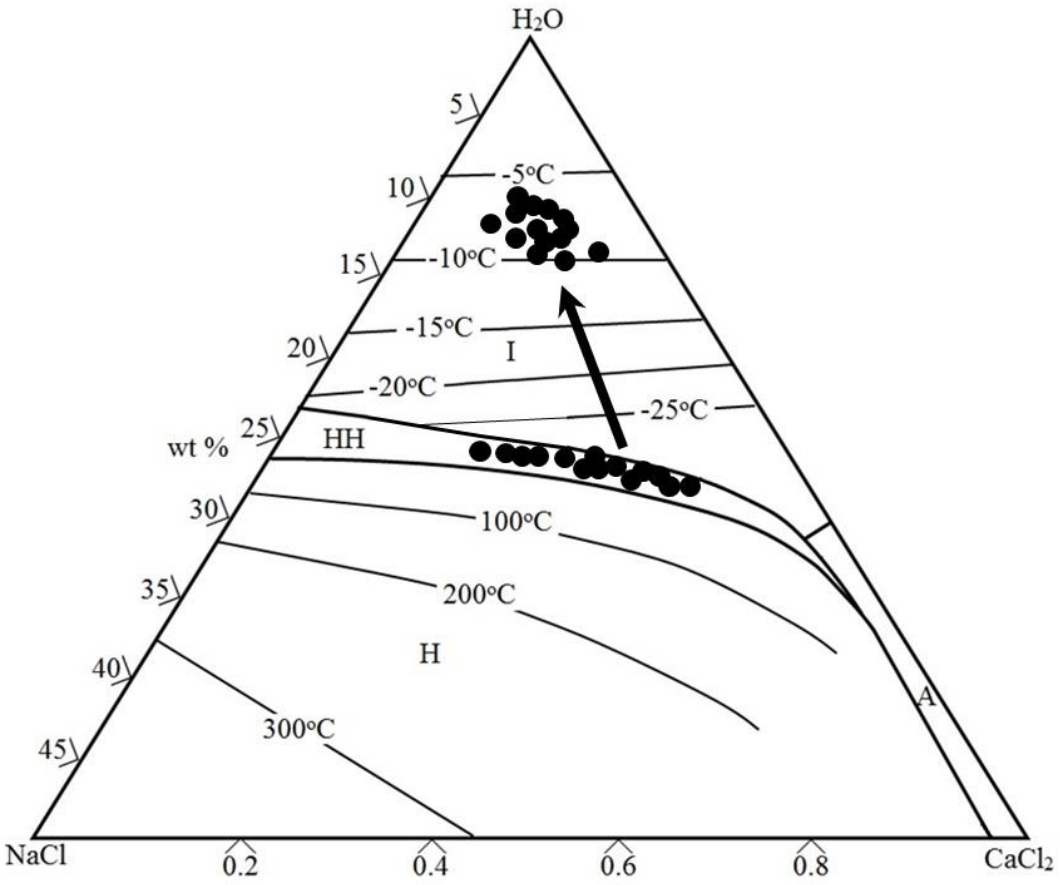
H2O
wt %
-5°C
-10°C
-15°C
-20°C
-25°C
100°C
200°C
300°C
I
HH
H
A
NaCl
CaCl2

Fig. 12

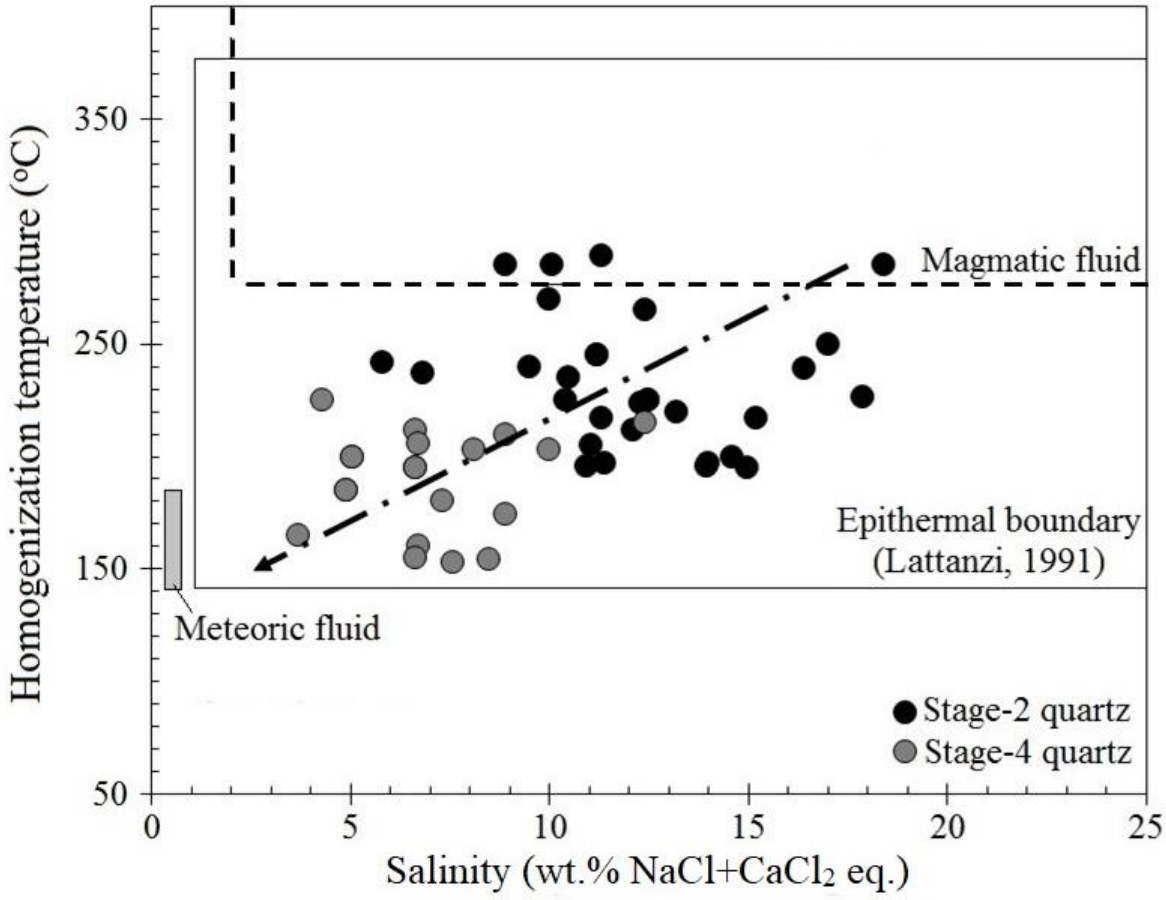

Fig. 13

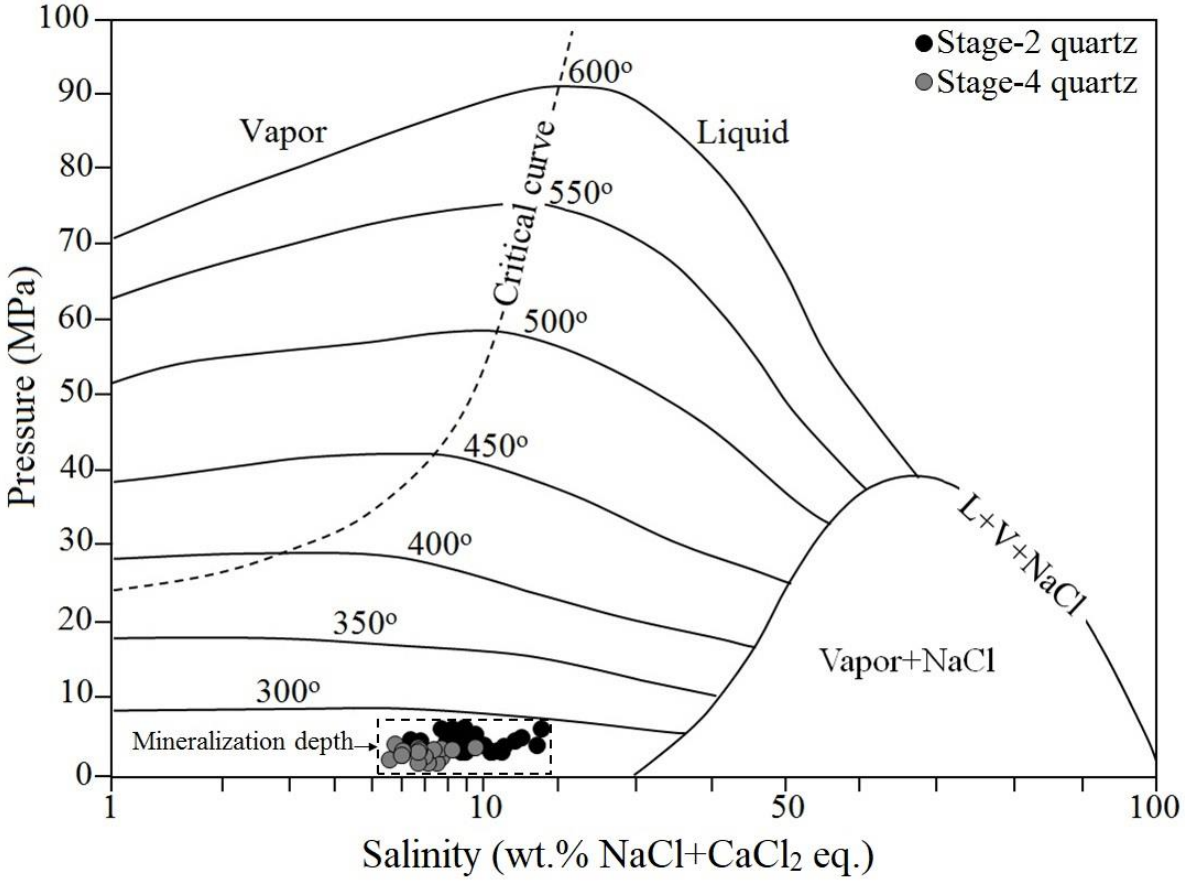

Fig. 14

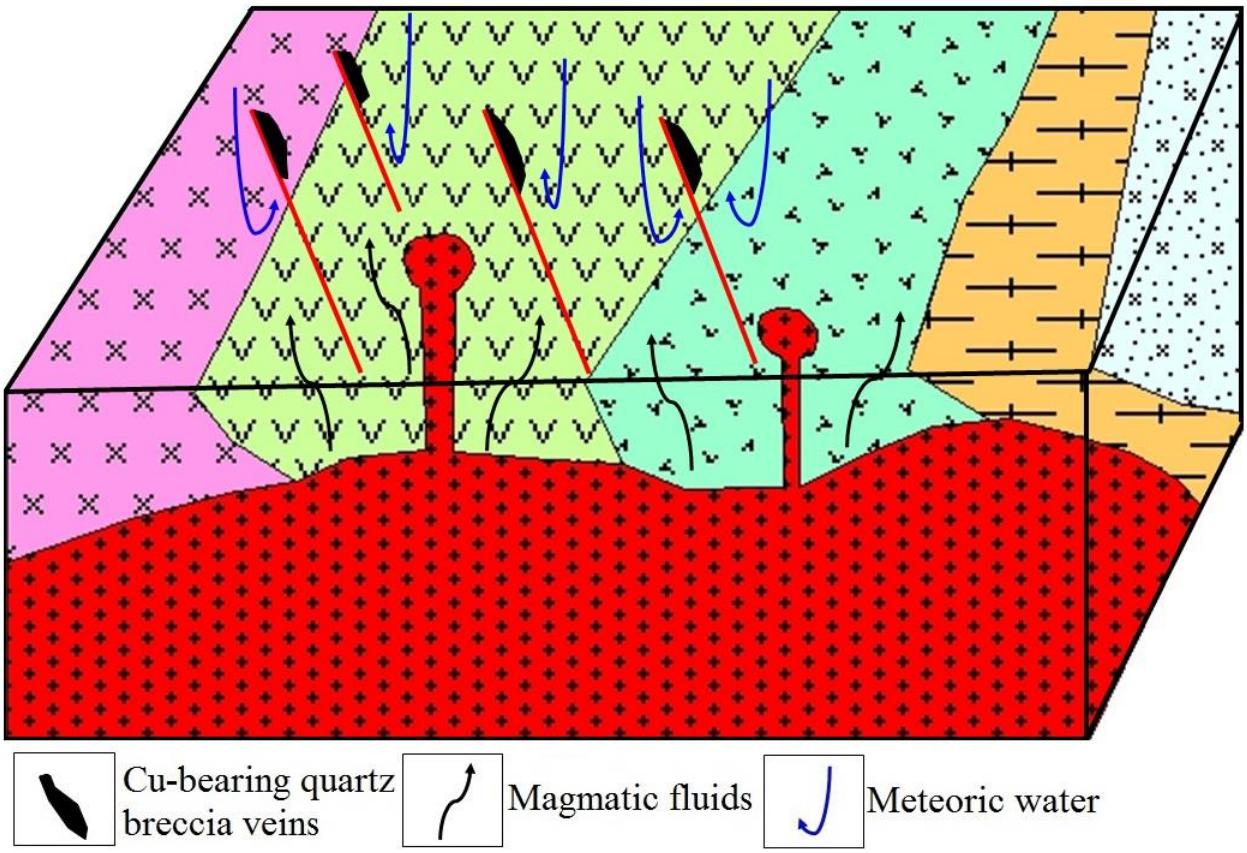

Fig. 15

Table 1

Criteria	Stage 1	Stage 2	Stage 3	Stage 4	Stage 5
Ore mineralogy	Minor pyrite and chalcopyrite	Major chalcopyrite and pyrite	-	Hematite	-
Alteration assemblages	Quartz, sericite/ illite	Quartz, sericite/illite	Quartz	Quartz	Chlorite
General occurrences/textures	Disseminated, veinlet	Vein- veinlet and breccia cements with colloform/ crustiform, cockade, vug infill and comb textures	Vein- veinlet, vug infill	Vein- veinlet, vug infill	Vein- veinlet, vug infill

Table 2

Mineral	T_e (°C)	$T_{m\text{-}ice}$ (°C)	$T_{m\text{-}hh}$ (°C)	T_h range (°C) low/mean/high	Salinity (wt.% NaCl+$CaCl_2$ equiv.)	ρ (g/cm^3)
Stage-2 quartz	−45 to −52	−3 to −16.4	−23 to −32	190/200/210 (5) 230/250/270 (23) 290 (2)	5.1–19.7 (12.4)	0.84–1
Stage-4 quartz	−30 to −35	−3 to −8.5	-	150/160/170 (5) 190/210/230 (15)	5.1–12.4 (6.6)	0.91–0.97

Note: number of measured inclusions in each fluid inclusion assemblage shown in parenthesis. T_e = first ice-melting, $T_{m\text{-}ice}$ = final ice-melting, $T_{m\text{-}hh}$ = hydrohalite melting, T_h = homogenization temperature.

Table 3

Sample no.	Stage of mineralization	Mineral	$\delta^{18}O_{quartz}$	$\delta^{18}O_{water}$ [a]	$\delta^{34}S_{sulfide}$	$\delta^{34}S_{H2S}$ [b]
AL-01	2	Chalcopyrite			–7.9	–8.1
AL-02	2	Chalcopyrite			–5.3	–5.5
AL-03	2	Chalcopyrite			–4.8	–5.0
AL-04	2	Chalcopyrite			–6.7	–6.9
AL-05	2	Chalcopyrite			–6.7	–6.9
AL-06	2	Chalcopyrite			–6.9	–7.1
AL-07	2	Quartz	13	3.6		
AL-08	4	Quartz	13.6	0.8		

[a] The $\delta^{18}O_{water}$ values were calculated using the fractionation equation of Méheut et al. (2007). [b] The $\delta^{34}S_{H2S}$ values were calculated using the fractionation equation of Li and Liu (2006). The mean values of T_h of fluid inclusions (Table 2) were used for calculation of isotopic compositions.